# REPORT DOCUMENTATION PAGE

Form Approved OMB NO. 0704-0188



| 1. REPORT DATE (DD-MM-YYYY) | 2. REPORT TYPE | 3. DATES COVERED (From - To) |
|---|---|---|
| 08-05-2019 | Final Report | 10-Aug-2015 - 9-Feb-2019 |

**4. TITLE AND SUBTITLE**
Final Report: Detection of Unresolved and Subpixel-Scale Anomalous Objects in Hyperspectral Imagery

**5a. CONTRACT NUMBER**
W911NF-15-1-0531

**5b. GRANT NUMBER**

**5c. PROGRAM ELEMENT NUMBER**
106012

**6. AUTHORS**

**5d. PROJECT NUMBER**

**5e. TASK NUMBER**

**5f. WORK UNIT NUMBER**

**7. PERFORMING ORGANIZATION NAMES AND ADDRESSES**
Alabama A&M University
4900 Meridian Street NorthWest
P. O. Box 429
Normal, AL 35762 -0411

**8. PERFORMING ORGANIZATION REPORT NUMBER**

**9. SPONSORING/MONITORING AGENCY NAME(S) AND ADDRESS (ES)**
U.S. Army Research Office
P.O. Box 12211
Research Triangle Park, NC 27709-2211

**10. SPONSOR/MONITOR'S ACRONYM(S)**
ARO

**11. SPONSOR/MONITOR'S REPORT NUMBER(S)**
67285-CS-REP.3

**12. DISTRIBUTION AVAILIBILITY STATEMENT**
Approved for public release; distribution is unlimited.

**13. SUPPLEMENTARY NOTES**
The views, opinions and/or findings contained in this report are those of the author(s) and should not contrued as an official Department of the Army position, policy or decision, unless so designated by other documentation.

**14. ABSTRACT**

**15. SUBJECT TERMS**

| 16. SECURITY CLASSIFICATION OF: | | | 17. LIMITATION OF ABSTRACT | 15. NUMBER OF PAGES | 19a. NAME OF RESPONSIBLE PERSON |
|---|---|---|---|---|---|
| a. REPORT | b. ABSTRACT | c. THIS PAGE | | | Barry Johnson |
| UU | UU | UU | UU | | 19b. TELEPHONE NUMBER 256-372-5587 |

# RPPR Final Report
as of 14-May-2019

Agency Code:

Proposal Number: 67285CSREP **Agreement Number: W911NF-15-1-0531**
**INVESTIGATOR(S):**


**Name:** Ph.D. Barry Johnson
**Email:** barry.johnson@aamu.edu
**Phone Number:** 2563725587
**Principal:** Y

**Name:** Sr. Chance Glenn
**Email:** chance.glenn@aamu.edu
**Phone Number:** 2563725560
**Principal:** N

**Name:** Ph.D. Kaveh Heidary Ph.D.
**Email:** kaveh.heidary@aamu.edu
**Phone Number:** 2563725587
**Principal:** N

**Name:** PhD Kenneth Sartor
**Email:** kenneth.sartor@aamu.edu
**Phone Number:** 2563728186
**Principal:** N

Organization: **Alabama A&M University**
Address: 4900 Meridian Street NorthWest, Normal, AL 357620411
Country: USA
DUNS Number: 079121448 EIN: 636001097


**Report Date:** 09-May-2019 Date Received: 08-May-2019
**Final Report** for Period Beginning 10-Aug-2015 and Ending 09-Feb-2019
**Title:** Detection of Unresolved and Subpixel-Scale Anomalous Objects in Hyperspectral Imagery
**Begin Performance Period:** 10-Aug-2015 **End Performance Period:** 09-Feb-2019
**Report Term:** 0-Other


Submitted By: Ph.D. Barry Johnson Email: barry.johnson@aamu.edu
Phone: (256) 372-5587



**STEM Degrees:** 1 **STEM Participants:** 5

**Major Goals:** The basic research objectives of this three-year project include the following:

1. to achieve an understanding of the relationship of the complexity of the hyperspectral image data cube and the degree of object anomaly from its immediate neighborhood that is detectable;
2. to investigate alternative algorithms to autonomously detect and locate subpixel anomalies in hyperspectral imagery;
3. to investigate the utility of applying means to optimize the selection of the spectral bands comprising the image data cubes to improve performance and reduction of computational resources;
4. to develop algorithms that detect and locate a subpixel-scale anomalous object when portions of the object are located in adjacent pixels;
5. to investigate algorithms that detect and locate an anomalous object when portions of the object are located in adjacent pixels and fill fully one or several pixels and/or portions thereof;
6. to investigate the impact upon Probability of Detection and False Alarm Rate resulting from the change in the output image from a focal plane array (FPA) as the optical image incident upon the FPA is shifted by subpixel amounts;
7. to investigate the efficacy of improving anomalous object detection performance if the Heidary-Johnson resolution enhancement algorithm is applied to the image data cube to synthetically enhance the data cube as if physical microdithering of the optical image on the FPA had occurred; and

8. to experimentally validate anomalous object detection algorithms.

The percent completion of each objective/task are as follows:

Objective 1: 100%.
Objective 2: 100%.
Objective 3: 100%.
Objective 4: 100%.
Objective 5: 100%.
Objective 6: 100%.
Objective 7: 100%.
Objective 8: 100%.

**Accomplishments:** See document in Upload section please.

**Training Opportunities:** Four undergraduate students and one graduate student were mentored in one or more areas such as how to use the radiometric equipment, basic theory of radiometry and how it applies to the project, experiment planning, computer programming, and image processing. The graduate student gained training in all of the above areas which helped him to be hired by a contracting firm that provides labor to the U.S. Army and prepares such people to transition to a civil service position in the U.S. Army. He has a couple of more classes to complete to earn a non-thesis M.S. Computer Science degree later this year. The undergraduate students participated in the project and received both mentoring and training in one or more of the above areas. Their participation enhances their attractiveness to both government and industrial employers. Over the duration of this Grant, several students have graduated with a B.S. degree and have been hired by commercial firms and while others are still working on earning their degrees.

**Results Dissemination:** The following paper was presented in April 2019 will be published in the Proceedings of the IEEE SoutheastCon 2019.

Kenneth Sartor, "Computational Enhancement in Locating Unknown Sub-Pixel Anomalous Sources in Hyperspectral Images," Proc. IEEE SoutheastCon (2019).

Over 100 downloads of the following paper were made from ResearchGate, Academia, and IJERS.

Kaveh Heidary and R. Barry Johnson, “Knowing the unknowable unknowns: subpixel anomalous source detection in hyperspectral imagery,” International Journal of Engineering Research & Science, 3(2), 52–65 (2017).

The following paper is to be submitted to Optical Engineering and expected to be published in 2019.

R. Barry Johnson and Kaveh Heidary, "Fidelity of Hyperspectral Imagery Produced by a Telecentric Phenoptic Hyperspectral Imaging System and its Impact on the Detection of Subpixel-Scale Anomalous Sources in Scenes of Unknown Characteristics," Optical Engineering (2019).

**Honors and Awards:** Nothing to Report

**Protocol Activity Status:**

**Technology Transfer:** Nothing to Report

**PARTICIPANTS:**

**Participant Type:** PD/PI
**Participant:** Ralph Barry Barry Johnson
**Person Months Worked:** 5.00 **Funding Support:**
Project Contribution:
International Collaboration:
International Travel:
National Academy Member: N

Other Collaborators:

**Participant Type:** Co PD/PI
**Participant:** Kaveh Heidary
**Person Months Worked:** 3.00 **Funding Support:**
Project Contribution:
International Collaboration:
International Travel:
National Academy Member: N
Other Collaborators:

**Participant Type:** Faculty
**Participant:** Kenneth Sartor
**Person Months Worked:** 2.00 **Funding Support:**
Project Contribution:
International Collaboration:
International Travel:
National Academy Member: N
Other Collaborators:

# Detection of Unresolved and Subpixel-Scale Anomalous Objects in Hyperspectral Imagery

**Final Report for August 10, 2015 through February 9, 2019**

## Prepared by


### Principal Investigator:

**Dr. R. Barry Johnson, FInstP, FOSA, FSPIE**
Senior Research Professor
Department of Physics, Chemistry and Mathematics
and
Department of Electrical Engineering and Computer Science
College of Engineering, Technology, and Physical Sciences

### Co-Principal Investigator:

**Dr. Kaveh Heidary**
Professor and Chair
Department of Electrical Engineering and Computer Science
College of Engineering, Technology, and Physical Sciences

### Faculty:

**Dr. Kenneth Sartor**
Assistant Professor
Department of Physics, Chemistry and Mathematics
College of Engineering, Technology, and Physical Sciences


## Table of Contents


1. Introduction 1

2. Specific Objectives 2

3. Major Activities 2

4. Significant Results 4

5. Key Outcomes or Other Achievements 6

Appendix 1 - Computational Enhancement in Locating Unknown Sub-Pixel Anomalous Sources in Hyperspectral Images 7

Appendix 2 - Fidelity of Hyperspectral Imagery Produced by a Telecentric Phenoptic Hyperspectral Imaging System and its Impact on the Detection of Subpixel-Scale Anomalous Sources in Scenes of Unknown Characteristics 16

# Detection of Unresolved and Subpixel-Scale Anomalous Objects in Hyperspectral Imagery

**Final Report for August 10, 2015 through February 9, 2019**

## 1. Introduction.

The Alabama A & M University (AAMU) is pleased to submit this Final Report on Detection of Unresolved and Subpixel-Scale Anomalous Objects in Hyperspectral Imagery funded under ARO Grant W911NF-15-1-0531. During this three-year investigation, the various goals were achieved adequately to have confidence that the enhanced detection method developed during the final reporting period is appropriate to continue research in a follow-on investigation to elevate the detection method next to a TRL 4 or TRL 5. Unlike the first detection method developed, the enhanced detection method appears to be well-suited for real-time implementation in custom hardware currently available. The reasons for this expectation are that (i) the enhanced detection algorithms are truly unknowing of the spatial and spectral content of both the hyperspectral scene and any anomalous objects in the scene, (ii) the decision threshold is relative insensitive, (iii) very tolerant to image corruption, (iv) excellent anomalous objects detection performance with extremely-low misclassifications, and (v) computations can be made in literally a totally parallel manner. The performance of the enhanced detection method will be presented in Appendix 2 of this Final Report.

In addition to the technical achievements of this investigation, significant and productive student involvement occurred. Two graduate students participated with one taking an industrial job upon graduation and the other took a job that leads to a civilian position in the U.S. Army Aviation and Missile Research, Development, and Engineering Center located at the Redstone Arsenal. A number of undergraduate students participated in training activities associated with this investigation. The academic performance of the graduate students was excellent as it was for some of the undergraduate students. Participation of these students in this Grant activity certainly enriched their learning experience at AAMU and should help prepare them for their careers.

Although having the ability to reliably detect anomalous sources on the ground when viewing from an aircraft, military or commercial, was recognized to be potentially significant in protecting the integrity of these aircraft, it is believed that additional dual-use applications may exist. In particular, this technology may aid in identifying anomalous areas in agriculture such as onset of disease or too dry/wet areas much sooner than current algorithms. Another potential application is identifying anomalous areas in manufactured parts such as impurities, microcracks, voids, and so on. Yet another potential application of this technology is to aid in identifying anomalous areas on the human body, such as skin diseases, diseases of the mouth, etc., and in locating anomalous areas in medical imagery. Such an adjunct tool may give the medical professional the ability to find problems far earlier than ever before, thereby potentially giving patients improved cure or survival expectations. In addition to detection of subpixel anomalous objects, the enhanced algorithms can also be implemented to allow detection of unresolved anomalous objects. Having real-time anomalous object detection capability will likely promulgate this technology into numerous applications yet not imagined.

## 2. Specific Objectives.

The basic research objectives of this three-year project included the following:

1. to achieve an understanding of the relationship of the complexity of the hyperspectral image data cube and the degree of object anomaly from its immediate neighborhood that is detectable;
2. to investigate alternative algorithms to autonomously detect and locate subpixel anomalies in hyperspectral imagery;
3. to investigate the utility of applying means to optimize the selection of the spectral bands comprising the image data cubes to improve performance and reduction of computational resources;
4. to develop algorithms that detect and locate a subpixel-scale anomalous object when portions of the object are located in adjacent pixels;
5. to investigate algorithms that detect and locate an anomalous object when portions of the object are located in adjacent pixels and fill fully one or several pixels and/or portions thereof;
6. to investigate the impact upon Probability of Detection and False Alarm Rate resulting from the change in the output image from a focal plane array (FPA) as the optical image incident upon the FPA is shifted by subpixel amounts;
7. to investigate the efficacy of improving anomalous object detection performance if the Heidary-Johnson resolution enhancement algorithm is applied to the image data cube to synthetically enhance the data cube as if physical microdithering of the optical image on the FPA had occurred; and
8. to experimentally validate anomalous object detection algorithms.

## 3. Major Activities.

AAMU is pleased to report that the above research objectives were accomplished although Objective 8 was not achieved in the manner originally anticipated. As was reported in the second Interim Report, the 16-color hyperspectral Surface Optics camera was experimentally determined to spectrally corrupt the hyperspectral image data cubes. This behavior was confirmed by a computer-based model of this camera design that was idealized to established the minimum spectral contamination of hyperspectral images. To understand the deleterious impact the camera induced spectral contamination can have upon the performance of the subpixel anomalous object detection algorithms, the camera model was used to create a transformation function that converts an original image hyperspectral data cube into a spectrally-corrupted hyperspectral data cube. As will presented in Appendix 2, the anomalous object detection performance [probability of detection (POD) and false alarm rate (FAR)] of the new detection algorithms were found to be essentially the same for the original and spectrally-corrupted hyperspectral images. How can this be? Perhaps the simple explanation is that the new detection algorithms are attempting to find anomalous subpixel-scale objects of unknown characteristics in a scene of also unknown characteristics. Remarkably, these newly developed algorithms appear to be very robust. In-depth analysis of the algorithms and performance is contained in Appendix 2.

**Appendix 1** contains a paper entitled "Computational Enhancement in Locating Unknown Sub-Pixel Anomalous Sources in Hyperspectral Images" that was presented at the IEEE SoutheastCon 2019 Meeting and will be published in the proceedings. This work addressed a method to decrease the computational load using the original Heidary-Johnson algorithm which requires the computation of the incongruence of a pixel with its neighboring pixels. The method used is an unsupervised learning algorithm that examines each pixel in the context of its immediate neighborhood without any a priori knowledge about the spatial and spectral characteristics of the expected background or potential anomalies. The image representing each of the spectral bands of the hyperspectral image under consideration is independently converted to a two-dimensional binary anomaly map. The composite anomaly map is then obtained by adding the entire set of anomaly maps to which a threshold is applied and detection decisions are subsequently made. Generation of the anomaly map requires that each of the spectral image planes of the data cube under evaluation be first converted to three pseudo-images, viz., Laplacian, Edge, and Turbulence and pseudo-images, which have the same spatial dimensions as the input image-plane. These are combined to form an incongruence map which is further transformed into the desired binary-valued anomaly map. Anomalies in the scene are searched for pixel-by-pixel while considering their surrounding neighborhood of pixels. Creation of the incongruence and binary-valued anomaly maps requires significant computations for each of the constituent pixels; however, it is possible to perform computations for pixels in parallel.

The objective of this computational enhancement investigation was to determine a method or methods to significantly reduce the computational requirements in creating the anomaly map. Two important decisions have to be made in computing the incongruence, viz., the selection of spectral bands and the incongruence threshold. Several findings were that (i) an Edge/Turbulence statistical evaluation of the pixel spectrums could be used to identify an "optimal" subset of spectral bands to utilize, (ii) the incongruence threshold can be determined using a small number of pixel patches and (iii) the incongruence threshold can also be determined using a small random selection of pixels over the entire image. The probability of detection (POD) and false alarm rate (FAR) for varying levels of contamination, incongruence, and band thresholding using a 224-band hyperspectral image were investigated. It was found that minimal degradation in performance occurred while significant decrease in computational load was observed. The result of this effort was an improved generic workflow for determination of subpixel anomalies in any hyperspectral image.

**Appendix 2** contains a paper entitled "Fidelity of Hyperspectral Imagery Produced by a Telecentric Phenoptic Hyperspectral Imaging System and its Impact on the Detection of Subpixel-Scale Anomalous Sources in Scenes of Unknown Characteristics" which is anticipated to be published in *Optical Engineering* later this year. The image fidelity produced by the sixteen band Surface Optics SOC716 VNIR hyperspectral camera was investigated by developing a simulation of a "perfect" telecentric hyperspectral phenoptic imager. This simulation assumed that the camera is aberration free other than for diffraction effects which can cause diffractive spectral contamination of the output data cube thereby degrading the image fidelity. The resultant transformations of input to output data cubes were used to investigate the impact on probability of detection (POD) and false alarm rate (FAR) of subpixel-scale anomalous sources in scenes having unknown characteristics. Counterintuitively, numerous simulations indicate that such spectrally contaminated output data cubes did not fundamentally degrade the POD and FAR performance of

Hyperspace Angle Mapping (HAM) detection algorithms used to locate anomalous subpixel-scale sources when compared to corresponding non-spectrally contaminated output data cubes.

The spectral corruption or blurring resulting from the design of the telecentric phenoptic hyperspectral camera was shown to be nontrivial and likely not useful for precision hyperspectral measurements. The principal question considered in this portion of the investigation was what impact does this camera's characteristic have on the detection of subpixel-scale anomalous objects. Intuitively, it would seem that such spectral corruption of a hyperspectral image would degrade the detection of anomalous objects. However, this examination strongly indicated that the new Johnson-Heidary HAM algorithmic method for anomaly detection is quite insensitive to spectral corruption of the image. The former Heidary-Johnson incongruence method for detection of subpixel-scale anomalous objects would inherently be more sensitivitive to spectral corruption of images than the new Johnson-Heidary HAM method. The reasons are that the incongruence method (i) requires the user to adjust, ad hoc, the threshold and selection of spectral bands, (ii) utilizes a constant threshold value, and (iii) is quite computationally intensive while the HAM method (iv) is a three tier process that greatly decreases the computational load, (v) has the user set a rather insensitive scaling factor, and (vi) autonomously determines the decision threshold for every pixel examined in the final tier. Furthermore, the detection and false alarms performance for the incongruence method is arguably grossly inferior to the HAM method.

The Johnson-Heidary HAM method for locating subpixel-scale anomalous objects was contrived to be generally oblivious to the nature of anomalous objects and to the structure of the image, i.e., the method's algorithms require no a priori knowledge of the anomalous objects or the image scene. The process examines individual 3x3 pixel kernels in the scene to determine if the core pixel is anomalous or not. Computationally, all of the kernels comprising the image can be processed in parallel if the software/hardware implementation is capable. Potentially, real-time scene analysis can be realized. In an example presented in Appendix 2, a complex hyperspectral image, obtained from the University of Manchester data bank, was analyzed. The scene contained over 1.3 million pixels and was transformed from a 32-band to 16-band data cube. Four randomly selected pixels from a different image were used as anomalies. Each was replicated 250 times for a total of 1000 anomalous objects. These anomalous objects randomly replaced pixels in the analyzed scene such that the total spectral power of the anomalous pixel and the original pixel were equal. This is considered the most stressing situation for any detection algorithm. The results obtained by applying the Johnson-Heidary HAM method were that 951 anomalous objects were correctly found and no false positives were declared. Also studied was the performance of the Johnson-Heidary HAM method when the anomalous source was only a fraction of the original pixel power.

**4. Significant Results.**

a. Continued growth in the understanding of the subpixel-scale anomalous source detection algorithms has been achieved by (i) extended algorithm development for subpixel-scale anomalous sources that lie partially in two, three, or four adjacent pixels, and algorithm development for unresolved anomalous sources having an extent of a small number of pixels.
b. Experimental testing of the telecentric phenoptic hyperspectral camera revealed non-trivial crosstalk between spectral channels. A computer model of the camera was developed and an end-

to-end simulation is under development for the purpose of understanding the impact of said crosstalk upon the anomaly detection algorithm performance.
c. Prior and continued investigations of subpixel-scale spatial phase vacillations and hyperspace angle mapping for spectrally-collapsing multispectral imagery have positively impacted development of extended algorithms for subpixel-scale anomalous source detection.
d. Both the project's undergraduate and graduate students earned a 4.0 GPA.

Significant results were obtained during the performance of this three-year Grant and are as follows:

1. At the beginning of the project, various anomalous object characteristics were induced into a reference hyperspectral scene to gain an understanding what disparity of scene pixels and anomalous objects are detectable. An insight was gained that was found useful in developing detection algorithms that differentiated an anomalous pixel from its immediate neighborhood of pixels.

2. Several alternative algorithms were investigated to autonomously detect and locate subpixel anomalies in hyperspectral imagery. Two methods were determined appropriate to study, viz., the Heidary-Johnson algorithm which requires the computation of the incongruence of a pixel with its neighboring pixels and the Johnson-Heidary HAM method that was found to be generally oblivious to the nature of anomalous objects and to the structure of the image.

3. Dr. Sartor lead the investigation into applying means, when using the Heidary-Johnson algorithm, to optimize the selection of the spectral bands comprising the image data cubes to improve performance and reduction of computational resources. See Appendix 1.

4. Modifications were made to the algorithms that detect and locate a subpixel-scale anomalous object when portions of the object are located in adjacent pixels. It was found that good detection performance was obtainable. See Appendix 3 in the 2017 Interim Report.

5. An investigation was made regarding modifying the algorithms that detect and locate an anomalous object when portions of the object are located in adjacent pixels and are considered unresolved, i.e., the anomalous object fill fully one or several pixels and/or portions thereof. It was found that good detection performance was obtainable. See Appendix 3 in the 2017 Interim Report.

6. The impact upon Probability of Detection and False Alarm Rate resulting from the change in the output image from a focal plane array (FPA) as the optical image incident upon the FPA is shifted by subpixel amounts was investigated. Due to the detection algorithms requiring no a priori knowledge of the anomalous objects or the image scene, the detection performance was observed to be rather robust.

7. The efficacy of improving anomalous object detection performance was investigated when the Heidary-Johnson resolution enhancement algorithm was applied to the image data cube to synthetically enhance the data cube as if physical microdithering of the optical image on the FPA had occurred. It was found that synthetic resolution enhancement did not improve detection

performance, but in general degraded performance. However, physical microdithering likely would improve performance.

8. Experimentally validation of anomalous object detection algorithms was not practicable due to technical issues with the Surface Optics hyperspectral camera owned by AAMU. Modeling of the telecentric phenoptic camera was accomplished to create an idealized model limited only by diffraction. Even so, it was found that an ideal camera of this type would cause significant spectral contamination on the resultant hyperspectral data cube. The Johnson-Heidary HAM method was applied to both an original hyperspectral image and its corresponding spectrally corrupted hyperspectral image. It was found that the POD and FAR were essentially the same for these images.

In addition, students were mentored in one or more areas such as how to use the radiometric equipment, basic theory of radiometry and how it applies to the project, experiment planning, computer programming, and image processing. Two graduate students participated in the project. One has graduated with a M.S. Computer Science degree and B.S. Electrical Engineering degree. He was hired by an industrial firm and is doing well in his job. The other graduate student earned a B.S. Electrical Engineering degree and has a couple of more classes to complete to earn a non-thesis M.S. Computer Science degree. He has been hired by a contracting firm that provides labor to the U.S. Army and prepares them to transition to a civil service position in the U.S. Army. He should complete his degree this year. Various undergraduate students participated in the project and received both mentoring and training. Several have graduated with a B.S. degree and have been hired by commercial firms and others are still working on earning their degrees.

**5. Key Outcomes or Other Achievements.**

Development of the Johnson-Heidary HAM method to detect subpixel-scale anomalous objects has been shown to perform remarkably well and appears to be implementable in hardware for real-time operation. The prime objective of the project was accomplished and should be funded to next develop the technology to TRL 3–4. Although research was performed for detecting anomalous objects using the Heidary-Johnson algorithms that residing in portions of adjacent pixels and for detecting unresolved anomalous objects that cover multiple pixels, further study needs to be performed to adapt the Johnson-Heidary HAM method for these cases. Future research suggested to be investigated includes (i) autonomous determination of the scaling constants $\kappa$ and $\chi$, (ii) detection when anomalous objects are partially in adjacent pixels, (iii) unresolved anomalous objects that extend over several pixels, (iv) coarse estimation of the nature of the anomalous objects such as if they are metal, natural material, plastics, etc. and (v) software/hardware implementation.

# APPENDIX 1

# Computational Enhancement in Locating Unknown Sub-Pixel Anomalous Sources in Hyperspectral Images

Kenneth Sartor
Department of Physics, Chemistry and Mathematics
Alabama A&M University
Normal, Alabama, USA 35762
Email: kenneth.sartor@aamu.edu

***Abstract*— The outcome of this research developed a new qualitative image processing approach to finding subpixel level anomalies in hyperspectral imagery. There were several steps involved in this process and there were 2 phases. First, anomalies were placed in the input hyperspectral image. In Phase 1, we chose a set of random chips or random pixels which were from the N x M x P hyperspectral image. Here the number of rows, columns, and bands of the hyperspectral image corresponds with N, M, and P respectively. A metric involving edge and turbulence is computed for each 3x3 neighborhood of pixels in the image. From this, a function is constructed where the domain (i.e. horizontal axis) is the band number and the range (i.e., vertical axis) is the corresponding "edge divided by turbulence" value after a first thresholding is applied. Throughout the paper, "edge divided by turbulence" is referred to as E/T. A second threshold is applied to this E/T function to determine the optimal bands to select from the hyperspectral image. In Phase 2, a transition into determining the probability of detection and probability of false alarm by adjusting the incongruence threshold H is performed. For this effort, a suite of Matlab tools was developed detailing information related to probability of detection (POD) and false alarm rate (FAR) for varying levels of contamination, incongruence, and band thresholding. A 224-band hyperspectral image was used as the evaluation image for this effort. The result of this effort was a generic workflow for determination of subpixel anomalies in any hyperspectral image.**

***Keywords—hyperspectral imagery, probability of detection, false alarm rate, subpixel, image processing***

## I. INTRODUCTION

This effort builds from the research described in [1]. The problem addressed in this original paper was finding objects (i.e., tanks) embedded on a sub-pixel level within an image by comparing the N-FINDER method [7] and the subpixel anomalous source detection algorithm(SASD). The author recommends the reader to review [1] if more details on the historical progression of this approach is needed. For the remainder of this paper, we'll refer to this SASD original work as the Heidary/Johnson approach. Figures 1 and 2 give a conceptual picture describing this new research effort. It should be noted that we have not reached the goal described in this diagram. The algorithms developed in this research help to progress towards the goals described in Figure 1. **The primary result of this new research effort is a workflow for semi-automatically determining subpixel anomalies from any hyperspectral image.** A 224-band hyperspectral image was used as the evaluation images for this effort.

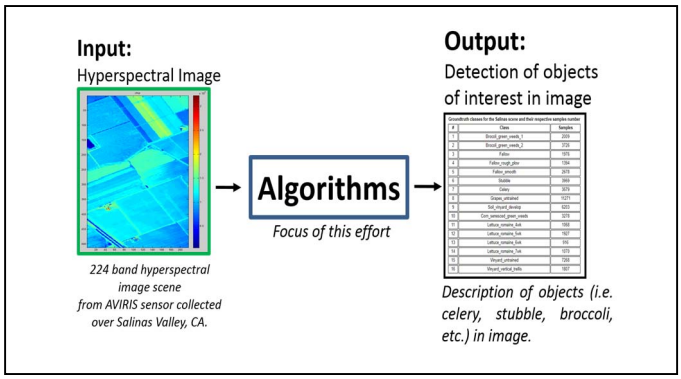


Fig. 1. Conceptual picture describing entire research effort. Ground truth table in figure taken directly from [2].

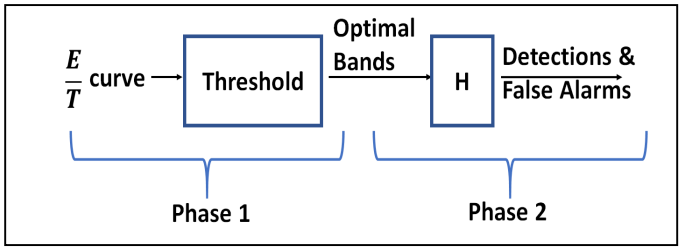


Fig. 2. Process for generating detections(inside of "Algorithms" box in Fig. 1)

In the original work [1], various graphs detailing probability of detection (POD) and false alarm rate (FAR) for varying levels of contamination, incongruence, and band thresholds were generated; the meaning of these terms will be reviewed in the next section. The Heidary/Johnson approach focused on subpixel anomalous source detection within a single pixel. Being able to solve this type of problem is very important in fields such as agriculture and defense. "It has been shown through many simulations, using actual HSI and RGB images,

that the SASD algorithm is capable of detecting subtle anomalies with high probability of detection and low false-alarm rates"(taken from page 10 in [1]).

For this new research effort, the original algorithms in [1] were re-implemented in MATLAB. The detection performance curves (i.e., True Positive Rate, False Negative Rate, False Positive Rate, True Negative Rate, and ROC curve) were generated for a selected image cube. The shape of the detection performance curves was compared to the shape of the original detection performance curves in [1]. If the shape was similar, then the author's implementation of the algorithms was deemed to be correct. After discussions with the original authors, it was verified that shape of the resultant curves from author's s/w implementation were consistent with the original algorithm implementation in [1].

The original paper indicated that a future research effort could be to "investigate spectral bands selection of image data cubes to improve performance and reduce computational resources" (taken directly from page 10 of [1])". **One purpose of the research results described in this paper is to fulfill that vision and idea.** Phase 1(see Figure 2) is a primary way how this work differs from [1].

After determining the "optimal" set of bands to process, the incongruence level H is chosen so that the P(DETECT) is maximized while the P(FAR) is minimized. This is accomplished by an iterative process of 1) either locally selecting random image chips or globally selecting random pixels across the entire image, 2) generation of "edge divided by turbulence" or E/T scalar values, 3) thresholding across these scalar values, 4) generation of E/T curve from the summation of thresholded scalar values, and 5) thresholding the E/T curve to obtain the optimal bands. The concepts of edge and turbulence as described in [1] will be reviewed in the next section.

This paper will go into details of the aforementioned local or global selection of image data, E/T computation per 3x3 neighborhood, summation of scalar E/T values after thresholding (i.e., E/T values less than one-standard deviation), generation of E/T function, thresholding of E/T function to obtain optimal bands, and determination of incongruence threshold H to properly balance P(Detect) & P(False Alarm). This process of adjusting the incongruence threshold H to maximize P(DETECT) and minimize P(False Alarm) is an iterative process.

## II. Background (Review of [1])

### A. Laplacian, Edge, Turbulence, & Incongruence Maps

"Applying the Laplacian filter (operator) to an input image is a well-known method for detection of abrupt intensity variations." (taken directly from page 3 of [1]). It is described by the following equation.

$$L_{mnp} = \left| -9D_{mnp} + \sum_{n'=n-1}^{n+1} \sum_{m'=m-1}^{m+1} D_{m'n'p} \right| ;$$

$$0 \le m \le M-1, \quad 0 \le n \le N-1, \quad 1 \le p \le P \tag{1}$$

where D and L denote respectively the source image plane data and its Laplacian pseudo image and M,N, & P are the number of pixels along the two spatial dimensions and the number of planes in the 3D data cube respectively (taken directly from page 3 of [1]).

"In order to avoid problems associated with segment boundaries that plague the Laplacian pseudo-image, an edge operator was developed." (taken directly from page 3 of [1]). It is described by the following equation.

$$E_{mnp} = \min_{\substack{m',n' \\ (m',n') \neq (m',n')}} \left| D_{mnp} - D_{m'n'p} \right| ;$$

$$m-1 \le m' \le m+1, \; n-1 \le n' \le n+1 \tag{2}$$

where E denotes edge pseudo image.

"The intensity at a particular pixel in the turbulence pseudo-image is directly proportional to the degree of chaos associated with intensities of its 9 neighboring pixels in the input image". (taken directly from page 3 from[1]). It is described by the following equation.

$$T_{mnp} = \sqrt{\frac{1}{7} \sum_{n'=n-1}^{n+1} \sum_{m'=m-1}^{m+1} \left( D_{m'n'p} - \mu_{mnp} \right)^2} ; \; (m',n') \neq (m,n) \tag{3a}$$

where T represents the turbulence pseudo-image.

$$\mu_{mnp} = \frac{1}{8} \sum_{n'=n-1}^{n+1} \sum_{m'=m-1}^{m+1} D_{m'n'p} ; \; (m',n') \neq (m,n) \tag{3b}$$

and $\mu_{mnp}$ is the neighborhood mean.

For each band (or layer) in the image cube, this is a ratio of the Laplacian-Edge Image product and Turbulence image (see equation 4a). Each band gets thresholded by incongruence threshold H to generate a binary image (see equation 4b).

$$\hat{I}_{mnp} = \frac{L_{mnp} E_{mnp}}{T_{mnp}} ; \; 0 \le m \le M-1, \; 0 \le n \le N-1, \; 1 \le p \le P \tag{4a}$$

$$I_{mnp} = \begin{cases} 1; \hat{I}_{mnp} \ge H \\ 0; \text{otherwise} \end{cases} \tag{4b}$$

where $\hat{I}$ and I denote, respectively, the continuously valued incongruence pseudo-image and the binary valued incongruence map. The user-specified incongruence threshold is H.

### B. Anomaly Mapping

The binary incongruence cube generated in previous step is summed, then thresholded by the band threshold Q (see equations 5a & 5b ).

$$\hat{A}_{mn} = \sum_{p=1}^{P} I_{mnp} \tag{5a}$$

$$A_{mn} = \begin{cases} 1; \hat{A}_{mn} \ge Q \\ 0; \text{otherwise} \end{cases} \tag{5b}$$

where $\hat{A}$ and A denote respectively the anomaly pseudo-image and anomaly map. Equations 6 through 8 describes how contamination was incorporated into the image where $f(m,n,p)$ is the original image, $R$ is the contamination factor, and $\hat{f}(m,n,p)$ is the contaminated hyperspectral image.

$$\hat{f}(m,n,p)=\begin{cases} f(m,n,p); & (m,n)\neq(m',n') \\ (1-R)f(m,n,p)+(\alpha)(R)c(p); & (m,n)=(m',n') \end{cases} \quad (6)$$

$$\alpha=\sum_{p=1}^{P} f(m',n',p) \Big/ \sum_{p=1}^{P} c(p) \quad (7)$$

$$\sum_{p=1}^{P} f(m,n,p)=\sum_{p=1}^{P}\left[(1-R_{m,n})f(m,n,p)+\alpha_{m,n}R_{m,n}c_{m,n}(p)\right] \quad (8)$$

"The [SASD] algorithm performs remarkably well since it detects the anomalies in the HSI evaluation image with high probability of detection and very low false-alarm rate. As expected, higher contamination factor and lower band-threshold both result in improved detection. It is observed that raising the value of incongruence-threshold leads to lower false-alarm rates. The value of the contamination factor has virtually no effect on false-alarm rate and the variations are due to the statistical nature of the problem." (taken directly from page 7 in [1]).

## III. Computational Enhancement Approach

### A. *"Image Cube Chip" approach*

This section describes the details of the new work accomplished that was not part of the original Heidary/Johnson approach described in [1]. In the first phase of the computational enhancement described in this paper, there is a determination of optimal bands. This is referred to as a local approach. To understand what is meant by Phase 1, please reference Figure 2 again. The optimal bands are found by generating a random set of image chips locally or generating a random set of image pixels across entire hyperspectral image globally. In this section, the focus is on the local image chip approach. This process is detailed in Figure 3.

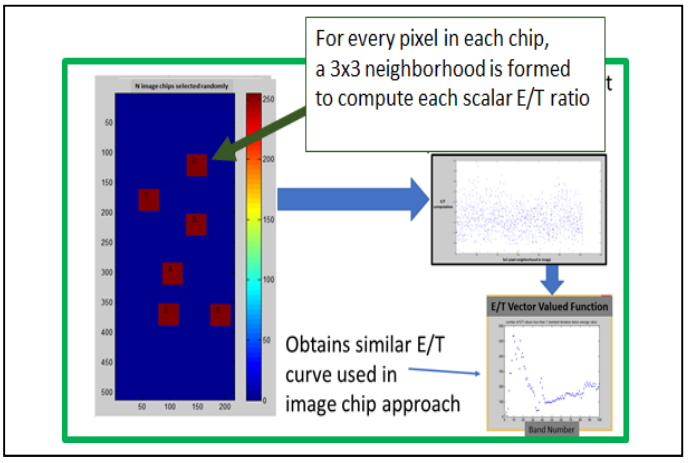


Fig. 3. Local Approach: Random Chips Chosen for 3x3 Neighborhood processing

For each of the P bands, there is an NxM image. Within this NxM image we select a chip and a 3x3 neighborhood of pixels is chosen around each pixel in the image chip (except at the borders). For this 3x3 neighborhood, the scalar value E is computed and the scalar value T is computed in accordance with Eqs. 2 and 3. **Recall that E denotes edge and T denotes turbulences as described in Eqs. 2 and 4, respectively.** This computation of E and T gets repeated for all pixels in the image chip. For this effort, we processed a 37x37 image chip which equates to (37-2)*(37-2) pixels values to give us a total of 1225 E and T value computations; these computation are shown in top right picture in Figure 3. Note that 2 is subtracted because image borders are not included. The ratio E/T was calculated for these 1225 E and T values of the $i^{th}$ band. This E/T equation can be thought of as a pseudo turbulence metric because it's similar to Eq. 4. Next, an average E/T value is computed for each band. A first threshold value being equal to the average E/T value minus one-standard deviation (of the average E/T value) was applied to the set of 1225 E/T scalar values in a particular band. This thresholding generates a subset of E/T values from the 1225 E/T values. The size of this subset was determined and this is the E/T value (i.e. range value) for current $i^{th}$ spectral band being processed (i.e. domain value). This process gets repeated for all P spectral bands to generate the E/T curve with length P where P is the number of hyperspectral bands; this curve is shown in the bottom right picture in Figure 3. The domain of this E/T curve is "hyperspectral band number" and the range is "number of E/T values that satisfied threshold criteria based on average E/T value". This process is also repeated for all random image chips selected; these are shown in the left-most picture in Figure 3. In Figure 3, we can see that six random image chips were generated. To obtain the "optimal" bands, a second heuristically determined threshold is then applied to this E/T curve in bottom right of Figure 3; one such thresholding in shown in Figure 4.

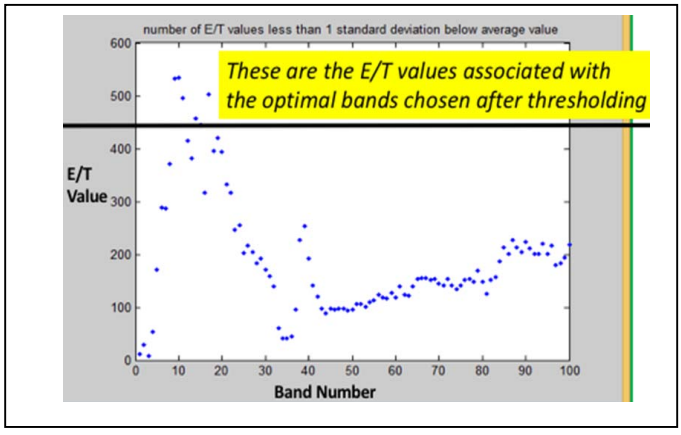


Fig. 4. Thresholding of E/T Curve to generate "optimal" bands

Here are some possible heuristic thresholding approaches that can be applied:

*1)* Aggregate **thresholded** E/T functions then threshold the aggregate E/T function. Here, the aggregation is simply done by summing all the E/T functions associated with each chip.

*2)* Aggregate **non-thresholded** E/T functions then threshold the resulting aggregate function

*3)* Do steps #1 or #2, then further post process by doing a heuristic or purely mathematical intersection of the resulting optimal bands. This heuristic process could be simply be "eye balling" the optimal bands associated which each chip and then aggregating manually based on subject matter expertise.

*4)* Choose a representative subset of the E/T functions and threshold heuristically or analytically.

In the second phase of this "image cube chip" local approach, we perform detection and FAR performance. Again, refer to Figure 2 to understand what is meant by Phase 2. For this approach, the anomaly was applied to every pixel in the hyperspectral image. Then the incongruence threshold H was varied until the desired balance between detection rate and FAR achieved. Because of extended processing time, only a subsection of the hyperspectral image was used to generate detection and FAR performance.

## B. *Random Pixel Selection approach*

In the first phase of this approach (Figure 2), there is a determination of optimal bands as we did for the local image chip approach. However, the random pixel selection is global in nature. As Figures 3 and 4 illustrates, the local and global approaches are identical except at the first step where the image data is selected.

The advantage of this random pixel selection approach is that one E/T curve utilizing "Random Pixel Selection" is generated as opposed to several. For this reason, no aggregation is necessary. The resulting E/T curve from this global approach was consistent with the aggregate E/T curve generated using "Image Chip" approach (i.e., local approach) as shown in the bottom right functions in Figures 3 and 4.

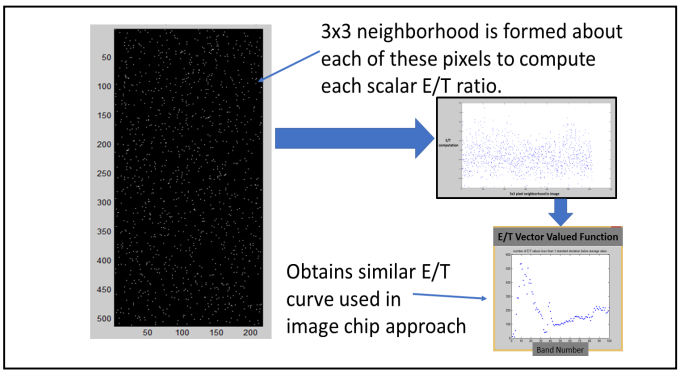


Fig. 5. Global Approach: Random pixels chosen for 3x3 Neighborhood processing

Some hyperspectral image cubes can contain a large number of bands and it is desirable to select a subset of these bands to process. As an example, the image cubes processed for this effort contained more than 200 bands. The hyperspectral image which exists as an (N*M*P) dimensional object in a very high dimensional space; specifically an (N*M*P+1)-dimensional space. This high dimensional object get mapped to an one-dimensional E/T function existing in a two-dimensional space. The discrete members of this E/T function get thresholded to obtain the set of "optimal" bands to process. If the number of bands is 224 and the optimal bands chosen is 10, then we go from processing an NxMx224 image cube to an NxMx10 image cube. This is the rationale for the need of this new qualitative approach and workflow in finding subpixel level anomalies in hyperspectral imagery.

The local approach reduces the amount of data to process. The global approach reduces the amount of data processing even more. With the local approach, we process several sets of M x N pixel neighborhoods corresponding which each local image chip. Whereas with the global approach, we process one set of M x N pixel neighborhoods across the entire image.

## IV. ANALYSIS

All of the data used in this effort came from [2]. Many experiments were run for this effort and no definitive conclusions were reached regarding the feasibility of the algorithms to reliably detect subpixel anomalies. **As stated before, the primary result of this effort was to formulate a workflow for quickly finding subpixel anomalies in hyperspectral imagery.** The purpose of this analysis section is to present a sampling of some of the results generated from various experiments.

The input image for this entire research effort is shown in Figure 6, the pixels were summed in the band direction. In other words, each pixel in this displayed image corresponds to the summation of spectral values across all P bands. The value for a single pixel can be estimated by looking at the color bar to the right of the image.

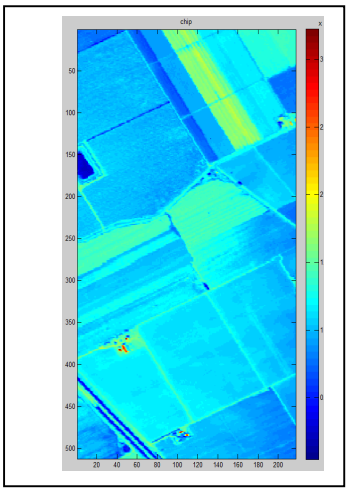

Fig. 6. Input Salinas Valley, CA hyperspectral image obtained from [2]

Figure 6 shows the 224-band hyperspectral image scene (which is called an image data cube) collected by the 224 band AVIRIS sensor collected over Salinas Valley, CA. The ground-level spatial resolution of each pixel is 3.7 meters. The area comprises 512 lines by 217 samples with 20 water absorption bands discarded. Image content includes vegetables, bare soils, and vineyard fields. The Salinas ground truth contains 16 classes and it is shown in Figure 8. Typical location of image

chips and corresponding image chip content that can be chosen from this image are shown in Figure 7.

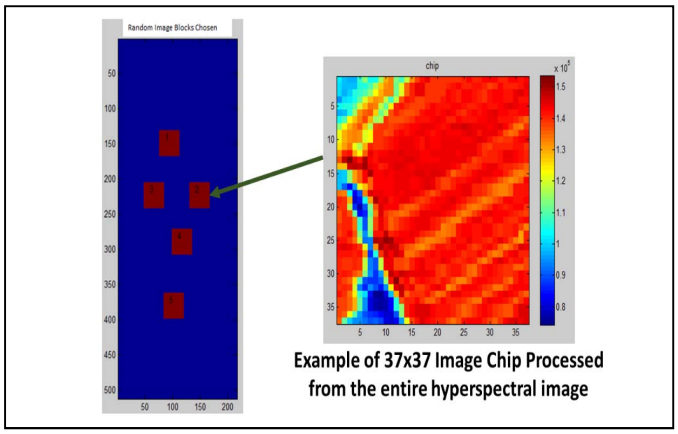


Fig. 7. Typical locations of image chips

For one of the experiments run, utilizing the algorithm described in Section III for chip 1 caused bands 5 through 9 to be chosen as the optimal cases. For chip 2, bands 25, 37, and 39 were computed to be the optimal choices. For chip 3, bands 5 through 12 were computed to be optimal. Table I details the remaining results. There was no mathematical intersection across all 5 image chips regarding optimal band selection. In other words, there were common optimal bands across all image chips. These results are in accordance with the high-level process described in Figure 2.

TABLE I. 'OPTIMAL' BANDS CHOSEN FOR EACH CHIP

| *Chip Number* | *Optimal Band Numbers* |
|---|---|
| 1 | 5 through 9 |
| 2 | 25, 37, 39 |
| 3 | 5 through 12 |
| 4 | 5 through 11 |
| 5 | 5 through 100 |

Table I illustrates that the selection of optimal bands is a semi-automatic process that requires some subject matter expertise. Even though there is no overlap between these resulting optimal bands, mathematically speaking, we still may want to inject our subject matter expertise and use optimal band selection results from all five chips. For example, we may decide to process bands 25, 39, 80 and 100 even though this doesn't represent a true mathematical intersection. This can be referred to as a heuristic intersection or aggregation (as opposed to mathematical intersection) based on subject matter expertise.

For this experiment, if we use a purely mathematical approach and not a heuristic one, then no optimal bands will be chosen!

Groundtruth classes for the Salinas scene and their respective samples number

| # | Class | Samples |
|---|---|---|
| 1 | Brocoli_green_weeds_1 | 2009 |
| 2 | Brocoli_green_weeds_2 | 3726 |
| 3 | Fallow | 1976 |
| 4 | Fallow_rough_plow | 1394 |
| 5 | Fallow_smooth | 2678 |
| 6 | Stubble | 3959 |
| 7 | Celery | 3579 |
| 8 | Grapes_untrained | 11271 |
| 9 | Soil_vinyard_develop | 6203 |
| 10 | Corn_senesced_green_weeds | 3278 |
| 11 | Lettuce_romaine_4wk | 1068 |
| 12 | Lettuce_romaine_5wk | 1927 |
| 13 | Lettuce_romaine_6wk | 916 |
| 14 | Lettuce_romaine_7wk | 1070 |
| 15 | Vinyard_untrained | 7268 |
| 16 | Vinyard_vertical_trellis | 1807 |

Fig. 8. Ground truth for Salinas Scene (taken directly from [2])

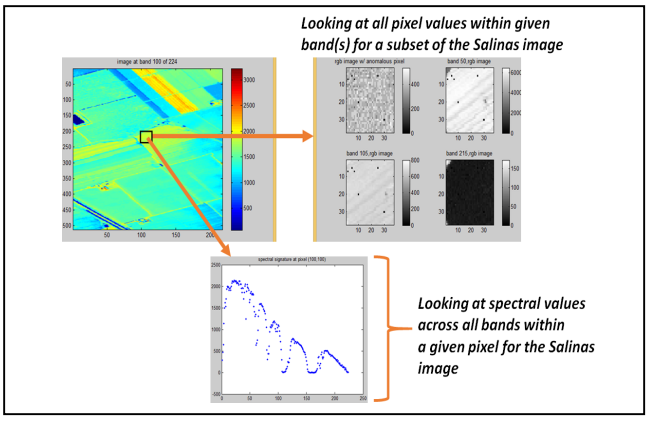


Fig. 9. Data understanding

The purpose of Figure 9 is to better understand the nature of the data being processed. The right portion of Figure 9 shows

bands 50, 105, and 215 of the 224 hyperspectral image of Salinas[2].

For another experiment, Table II illustrates that the numbers of optimal bands chosen can vary significantly on a chip by chip basis and as Figure 2 implies, the threshold has an impact on this computation.

TABLE II. RESULTS PROCESSING TO GET 'OPTIMAL' BANDS

| *Chip Number* | *Number of optimal bands* |
|---|---|
| 1 | 11 |
| 2 | 3 |
| 3 | 15 |
| 4 | 17 |
| 5 | 89 |
| 6 | 57 |

The probability of false alarm P(FAR) is found by integrating from threshold to end of the noise curve in theoretical picture (Figure 11) in the leftward direction. The probability of detection P(Detect) is found by integrating from threshold to end of signal curve in the rightward direction. The purpose of the ROC (Receiver Operating Characteristic) curve shown in Figure 10 is to show the trade-off between P(Detect) and P(False Alarm) when incongruence H is used as the parameter.

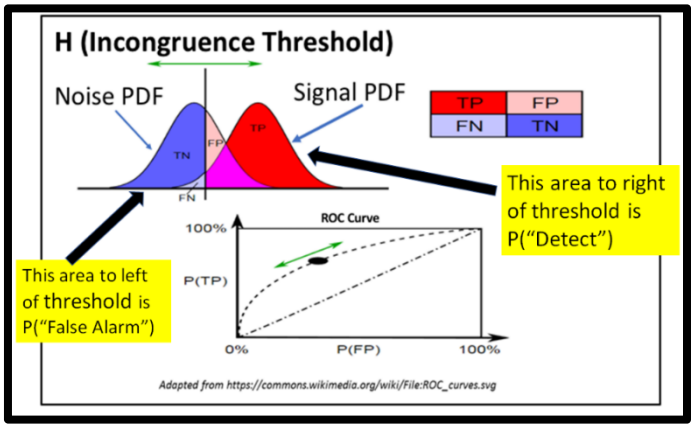


Fig. 10. Theoretical Meaning of Incongruence Threshold H (adapted from [10])

In order to determine false alarm rate, we set contamination equal to 0, decide on number of bands (i.e. 11 out of 11 for now as shown in Table 2 for chip 1), then determine via multiple runs the value of H (which is the threshold in Figure 18) that brings the false alarm rate to zero. This will be the value of H. We use this value of H for all the runs.

If we change the number of bands, then this also changes H. Figure 2 clearly implies this. False alarm computation is a function of H incongruence threshold and Q band threshold. A higher Q means a lower H is needed and vice versa. Said in a more rigorous way, FA = f(H) and H=g(Q) therefore the composite function can be seen as FA = f(g(Q) where g corresponds to the inner function that describes H as a function of Q. It appears that this H=g(Q) function can be modeled as an exponential (or logarithmic) function; more investigation is needed though to reach a definitive conclusion on this. Reducing the number of bands lowers the criteria which means false alarms will go up. This also implies that we'll need to increase H to get rid of those false alarms.

Tables III, IV, and V are examples of results from processing flow from illustrated in Figures 1 & 2. These tables highlight that even though the algorithms tell us there are a certain number of optimal bands, we can still further reduce this number of optimal bands by using our subject matter expertise.

TABLE III. PROBABILITY DETECT AND FAR RESULTS

| *Number of Optimal bands* | *P (DETECT)* | *P (FAR)* |
|---|---|---|
| 7/11 | 95.4% | 13.1% |
| 9/11 | 59.8% | 9.4% |
| 11/11 | 5.4% | 4.9% |
| 4/11 | 99.6% | 22.3% |

TABLE IV. PROBABILITY DETECT AND FAR RESULTS

| *Incongruence Level H* | *P(FAR)* |
|---|---|
| 0 | 100% |
| 1.00E-15 | 10% |
| 0.0001 | 10% |
| 0.01 | 9.80% |
| 0.1 | 9.60% |
| 1 | 7.40% |
| 5 | 4.90% |
| 50 | 0.16% |
| 75 | 0.08% |
| 100 | 0% |
| 500 | 0% |

TABLE V. IMPACT OF INCONGRUENCE LEVEL ON DETECTION AND FAR

| *Incongruence Level H* | *Number of Optimal bands* | *Contamination Level R* | *P(DETECT)* | *P(FAR)* |
|---|---|---|---|---|
| 75 | 7/11 | 0% | NA | 0.49% |
| 100 | 7/11 | 0% | NA | 0.33% |
| 200 | 7/11 | 0% | NA | 0% |
| 75 | 7/11 | 100% | 59.18% | NA |
| 200 | 7/11 | 100% | 26.45% | NA |
| 75 | 4/11 | 0% | NA | 1.55% |
| 100 | 4/11 | 0% | NA | 0.6% |
| 200 | 4/11 | 0% | NA | 0% |
| 200 | 4/11 | 100% | 76.2% | NA |
| 200 | 4/11 | 100% | 78.5% | NA |
| 75 | 1/11 | 0% | NA | 3.8% |
| 75 | 1/11 | 0% | NA | 1.9% |
| 200 | 1/11 | 0% | NA | 0.24% |
| 75 | 1/11 | 100% | 91.3% | 3.8% |
| 200 | 1/11 | 100% | 78.6% | NA |

In summary, the optimal bands chosen is a function of the image cube content. From this set of optimal bands automatically generated, a subset was selected heuristically. This can be viewed as a heuristic as opposed to a mathematical intersection as mentioned multiple times before in this paper.

The random pixel selection is shown in Figure 4. This is an alternative to the random image cube block selection shown in Figure 3. As shown in Figure 6, a random 3x3 neighborhood is constructed about each of the randomly chosen pixels across the complete hyperspectral image. Next, the E(i,j) and T(i,j) scalar values are computed from each 3x3 neighborhood based on equations 2 and 3. This process is repeated for all 1225 3x3 randomly chosen pixels across the entire hyperspectral image using the aforementioned thresholding process.

As Figures 3 & 5 shows, the results between the random block selection and random pixel selection are consistent because the E/T curves generated by both approaches are consistent. The theoretical reasons why the E/T curve from the random image block (aggregate) and random pixel approaches are consistent can be investigated in a future effort.

Figure 11 (example of E/T Curve for one of N Chips) is an example of one of the E/T functions that can get aggregated to obtain another E/T function. This aggregate E/T function can be thresholded again to obtain the optimal bands.

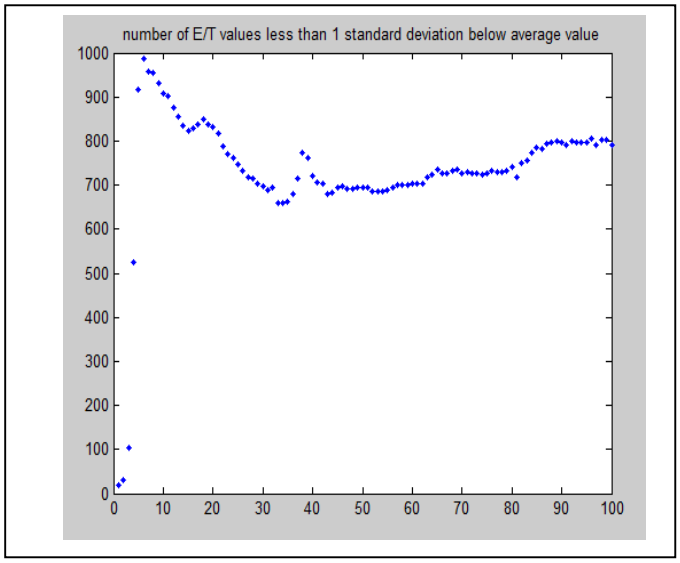


Fig. 11. E/T Curve Generated by Random Pixel Selection

"In order to assess the efficacy of the subpixel anomalous source detection algorithm, a large number of evaluations were performed on actual images. Performance simulations were carried out on a wide selection of RGB images, a small subset of which is presented here, as well as two actual ninety-band hyperspectral data cubes. Numerous types of synthetic anomalies were transplanted into actual images in order to construct contaminated images constituting the simulated ground truth for each evaluation. The detection algorithm was applied to the contaminated evaluation images without any a priori knowledge about the image statistics and the locations and makeup of potential anomalies. The results pertaining to the coordinates of suspected anomalous pixels, as determined by the algorithm, were then compared to the ground truth for each evaluation and the detection/FA rates were subsequently computed for each case. As will be observed from the following examples, the algorithm is capable of detecting subtle anomalies in complex imagery with high probability of detection and low false-alarm rate. For comparison purposes the performance of the Boeing Enhanced N-FINDR algorithm, a subpixel HSI anomalous-source detection method, is also presented in Section 3" (directly taken from [1]).

To detect anomalies, the H incongruence threshold was moved to the far right (see Figure 12 on next page). Theoretically speaking, the resulting detections should be equivalent to the true anomalies. For the experiment run, this was not the case so further investigation is needed. This could be the topic for a future research effort.

Fig. 12. Process for anomaly detection (adapted from [10])

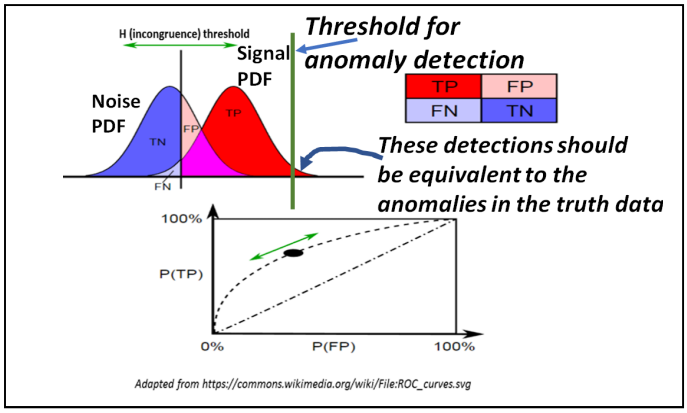


## V. CONCLUSIONS

In this paper, a generic image processing work flow was developed that can automatically determine optimal bands from an arbitrary hyperspectral image and compute detections of subpixel anomalies (Figure 1). Results were generated for several cases including varying contamination levels, incongruence threshold, band threshold, image cube sizes, and anomaly placement. Future work can include doing an in-depth analysis of the results of these simulation runs and determining approaches to improve the speed of the algorithms. Also, work can be done on methodologies which dynamically set the incongruence level H.

The E/T band selection method and random sampling method was observed to significantly reduce the computational complexity and load while still yielding approximately the same POD and FAR performance compared to the method used in [1].

## ACKNOWLEDGMENT

This research was funded by the Army Research Office (W911NF-15-1-0531). The author thanks Dr. R. Barry Johnson and Dr. Kaveh Heidary of the Alabama A&M University Department of Electrical Engineering and Computer Science for their review and comments regarding this paper and throughout this research effort in general.

## REFERENCES

[1] K. Heidary, R.B. Johnson, "Knowing the unknowable unknowns: subpixel anomalous source detection in hyperspectral imagery", International Journal of Engineering Research & Science, vol. 3, pp. 52–65, (2017)

[2] Hyperspectral Remote Sensing Scenes from Grupo de Inteligencia Computacional http://www.ehu.eus/ccwintco/index.php?title=Hyperspectral_Remote_Sensing_Scenes (accessed August 21, 2017)

[3] D. Manolakis, D. Marden, and G. A. Shaw, "Hyperspectral Image Processing for Automatic Target Detection Applications," Lincoln Laboratory Journal, Vol. 14, No. 1, 79–116 (2003).

[4] M. E. Winter, "N-Finder: An algorithm for fast autonomous spectral end-member determination in hyperspectral data," Proc. SPIE, Vol. 3753, *Imaging Spectroscopy V*, 266–275 (1999).

[5] D. W. J. Stein, S. G. Beaven, L. E. Hoff, E. M. Winter, A. P. Schaum, and A. D. Stocker, "Anomaly Detection from Hyperspectral Imagery," IEEE Signal Processing Magazine, Vol. 19, No. 1, 58–69 (2002).

[6] Y. Cohen, D. G. Blumberg, and S. R. Rotman, "Subpixel hyperspectral target detection using local spectral and spatial information," J. of Appl. Remote Sensing, Vol. 6, 063508 (2012).

[7] Q. Du, N. Raksuntorn, N. H. Younan, and R. L. King, "Variants of N-FINDR Algorithm for Endmember Extraction," Proc. SPIE, Vol. 7109, *Image and Signal Processing for Remote Sensing XIV*, 71090G-1–8 (2008).

[8] D. Manolakis, C. Siracusa, and G. Shaw, "Hyperspectral subpixel target detection using linear mixing model," IEEE Transactions on Geoscience and Remote Sensing, Vol. 39, No. 7, 1392–1409 (2001).

[9] D. Landgrebe, "Hyperspectral image data analysis," IEEE Signal Processing Magazine, Vol. 19, No. 1, 17–28, (2002).

[10] Wikipedia article and image on "Receiver operating charateristic". https://en.wikipedia.org/wiki/Receiver_operating_characteristic https://en.wikipedia.org/wiki/Receiver_operating_characteristic#/media/File:ROC_curves.svg (accessed March 17, 2019)

# APPENDIX 2

# Fidelity of Hyperspectral Imagery Produced by a Telecentric Phenoptic Hyperspectral Imaging System and its Impact on the Detection of Subpixel-Scale Anomalous Sources in Scenes of Unknown Characteristics

R. Barry Johnson and Kaveh Heidary
Department of Electrical Engineering and Computer Science
Alabama A&M University, Normal, Alabama
barry.johnson@aamu.edu and kaveh.heidary@aamu.edu

**Abstract:** The image fidelity produced by the sixteen band Surface Optics SOC716 VNIR hyperspectral camera has been investigated by developing a simulation of a "perfect" telecentric hyperspectral phenoptic imager. This simulation assumed that the camera is aberration free other than for diffraction effects which can cause diffractive spectral contamination of the output data cube thereby degrading the image fidelity. The resultant transformations of input to output data cubes was used to investigate the impact on probability of detection (POD) and false alarm rate (FAR) of subpixel-scale anomalous sources in scenes having unknown characteristics. Counterintuitively, numerous simulations indicate that such spectrally contaminated output data cubes did not fundamentally degrade the POD and FAR performance of Hyperspace Angle Mapping (HAM) detection algorithms used to locate anomalous subpixel-scale sources when compared to corresponding non-spectrally contaminated output data cubes.

**Key Words:** Hyperspectral, hyperspectral camera, phenoptic camera, anomalous source detection, spectral contamination

## 1. Introduction

In support of a research project to detect anomalous unresolved or subpixel-scaled objects in hyperspectral imagery, a Surface Optics SOC716-VNIR Hyperspectral Imaging System was used to gather imagery for evaluation of detection algorithms.[1] Determination, by field testing, of the spectral fidelity of SOC716-VNIR produced hyperspectral imagery was accomplished. It was observed that spectral contamination appeared in some imagery which raised concern about the subpixel anomalous source detection (SASD) algorithms' effectiveness on potentially spectrally-degraded or contaminated imagery. The SOC716-VNIR is a high-speed imaging system utilizing low-noise silicon-based CCD, SOC's patented 3D Imaging Core, and capture software. The SOC716-VNIR can simultaneously record sixteen spectral bands forming 512 by 512 by 16-pixel image data cubes at a rate of up to 28 frames (data cubes) per second.[2] The system's spectral response covers the visible and NIR spectral range from 450–950 nm and can be used in normal lighting conditions with variable exposure times and gain. The camera is a telecentric phenoptic

[1] Kaveh Heidary and R. Barry Johnson, "Knowing the unknowable unknowns: subpixel anomalous source detection in hyperspectral imagery," *International Journal of Engineering Research & Science*, **3**(2), 52–65 (2017).
[2] David B. Cavanaugh, James M. Lorenz, Nora Unwin, Mark Dombrowski, and Paul Willson, "VNIR hypersensor camera system," *Proc. SPIE*, Vol. 7457, 74570O (2009).

configuration having sixteen spectral filters which form a four by four matrix in the camera's entrance pupil/stop.

The question addressed in this investigation was to determine if this type of hyperspectral camera could provide imagery that would yield equivalent results to non-spectrally-contaminated imagery when evaluated by the SASD detection algorithms based upon the Hyperspace Angle Map (HAM) concept discussed in Section 4. Although field testing of the SOC716-VNIR provided some insight, the operational behavior of the imager was felt to be slightly imperfect, i.e., residual spatial and chromatic aberrations in addition to diffraction effects. To determine the best possible performance of this class of imager, a "perfect" computer model of the camera was developed such that the only residual imperfection was diffraction. This approach established the ultimate image fidelity limitation of such camera configurations. Further, the model provided a transfer matrix that transformed the hyperspectral data for each scene or input pixel into the corresponding image or output pixel hyperspectral data including the spectral contamination in the output pixels and those proximate to it. This is a complex contamination process that doesn't appear to have a method to recover the original scene, i.e., no inversion method is evident.

In the following sections, a brief summary of the field test is presented, the camera model development and transfer matrix are discussed, an improved SASD algorithm is explained and is incorporated in the simulation computer program, and POD and FAR results of simulations of various scenes and anomalous sources are provided. Intuitively, it was anticipated that the probability of detection (POD) and false alarm rate (FAR) performance for locating subpixel-scale anomalous sources in scenes, both having unknown characteristics, would be significantly decreased; however, this was remarkably not the case.

## 2. Field Test

The images of a distant single white-light point-source were taken using the SOC716-VNIR. Each image data cube comprised sixteen 512 by 512 images having 12-bit resolution. In addition, the system generated an RGB image. To determine the amount of spectral contamination, a mask set was constructed so that only a single filter illuminated the detector array. By examining the resultant data cubes, spectral contamination could in principle be determined. A total of four masks were constructed that fit over the filter holder of the SOC716-VNIR (see Figure 1). This made it possible to rotate each mask by 90-degree angles to expose one band filter at a time for a total of four bands per mask. Although hyperspectral images produced by the SOC716-VNIR looked acceptable when viewing general scenes (see Figure 2), a surprising result of the point-source field test was that significant spectral spillage were observed that were spectral band dependent. Explicitly stated, the image of the point source was seen in superpixel of the output data cube where expected, but the source was seen in many of the other bands causing spectral contamination of the output data cube. As will be explained, the reason for this contamination is due to diffraction and the fundamental configuration of the camera. Nevertheless, the SOC716-VNIR camera can be useful for a variety of hyperspectral data gathering tasks.

Figure 1. Photograph of the SOC716-VNIR camera shows the spectral filters in their 4x4 matrix holder.

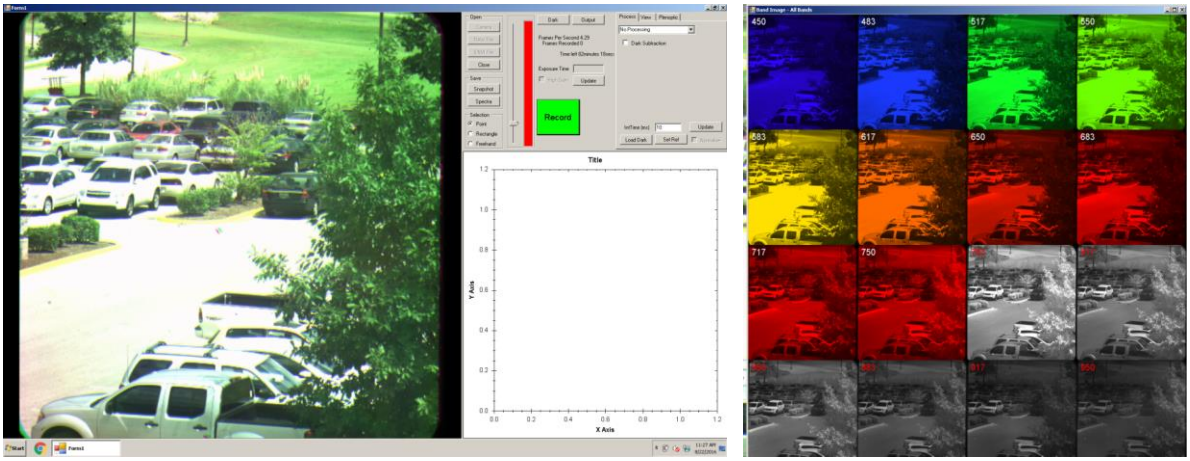


Figure 2: Typical display of the SOC716-VNIR showing (a) RGB image and (b) spectral images.

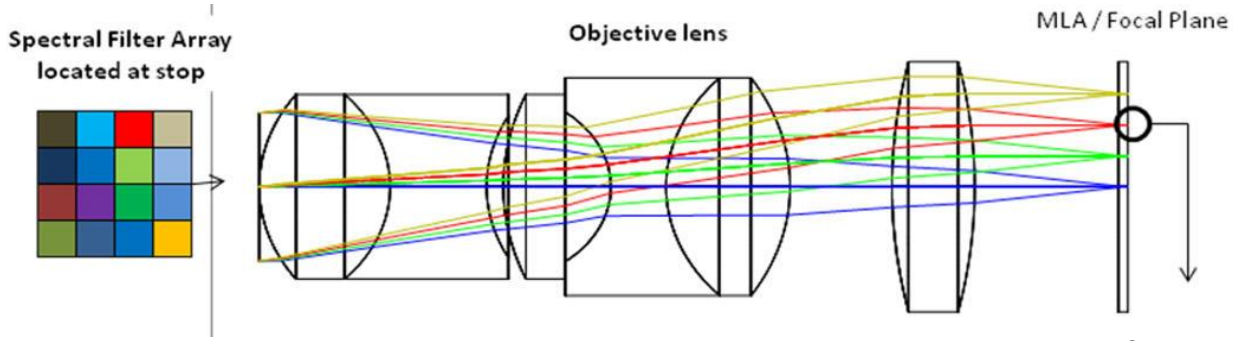


Figure 3. Basic optical configuration of the telecentric plenoptic hyperspectral camera.[3]

## 3. Idealized Camera Model

The Model SOC716 is a telecentric plenoptic hyperspectral camera that covers the 450-950nm spectral region in 16 bands and produces 512x512x16 12-bit data cubes at up to 27 fps. The

[3] Figure 3 after Figure 2 in footnote 2.

detector is a 4K by 4K Si-CCD which is configured to provide sixteen 512x512 arrays with each corresponding to a separate spectral band. Figure 3 illustrates the optical configuration of the camera.

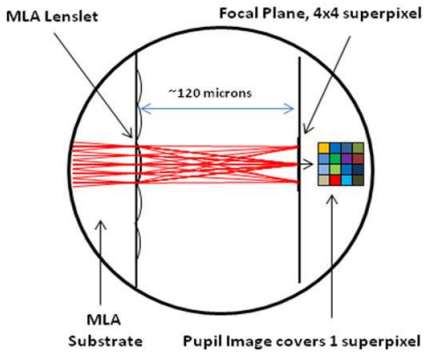


Figure 4. Imaging of the Mosaic Filter Array (spectral filter array) onto the CCD by the microlens array (MLA).[4]

For this system, the imaging lens needs to be telecentric, thereby causing the principal rays from the scene to be orthogonal to the image plane. As is typical, the optical system is made telecentric by placing the stop at the front focal plane which also is the entrance pupil. The spectral filters are located at the stop/entrance-pupil of the optical system. An image of the scene is formed at the image plane of the objective lens. In order for an array of superpixels to be formed, a microlens array (MLA) is placed at the image plane. The MLA then images the spectral filter array onto the CCD detector array which further means that the detector array is located at the exit pupil of the optical system. Figure 4 shows this arrangement. It is evident that the 4K by 4K CCD is optically divided into an array of 512x512 superpixels where each detector in a superpixel's 4x4 array of detectors represents a specific spectral band. This is a very clever way to simultaneously form sixteen spectral images of a scene in contrast to scanning the scene sixteen times, once in each spectral band.

So, what are the limitations of using this camera approach for even an idealized system? Simply put, diffraction and slight defocus. Although the custom-designed 85-mm focal length objective lens is about F/2.4, the actual image of a scene is formed using a square-aperture F-number of not less than F/13.5.[5] A plenoptic camera is a bit unusual and deserves a bit of explanation.[6] As mentioned previously, a superpixel can be considered to be imaged onto the scene in a geometrical sense. However, the spectral light from each pixel in the scene is incident upon the spectral filter array and the flux passing through each filter is imaged onto a corresponding detector located within the matching superpixel. For the SOC716 configuration, this would be an ideal system if considered geometrically; however, diffraction causes significant complications in accurately

[4] Figure 4 provided courtesy of Surface Optics Corporation.

[5] The area of an inscribed square in a circle is about 64% of the area of the circle. The area of each "micro spectral camera" optical system is therefore 1/16$^{th}$ time 64% (or 4%) of the area of the objective lens. The side width of the largest square filter is $(0.04*\pi/4*D^2_{\text{objective lens}})^{1/2} = 0.177\ D^2_{\text{objective lens}}$. Hence, the smallest value of filter F-number becomes 2.4/0.177 = 13.5. However, as will be explained, the detector pitch (distance between detector elements of 7.4 µm) results in a spectral filter pitch of 5.25 mm and the filter F-number becomes 16.2.

[6] Section 2.2, Christopher Hahne, "The Standard Phenoptic Camera," Section 2.2, Doctoral Dissertation, University of Bedfordshire (2016).

measuring the spectrum of the scene because the diffraction causes the flux intended for a given detector to be spread over nearby detectors within its superpixel or proximate superpixels.[7] Consequently, any flux "spillage" onto detectors spatially surrounding the intended detectors will result in an incorrect spectral measurement of the scene. For the purpose of this investigation, all of the detectors comprising the CCD are considered to be equally responsive to flux within the entire 450-950 nm spectral region. Surface Optics Corp. (SOC) has attempted to resolve this issue by calibrating the camera and then correcting the output hyperspectral data cube. They achieve this calibration by viewing a known large area source of uniform radiance. A calibration data cube is generated for each spectral band by blocking all but the appropriate filter when taking the data. With this information, they now have sixteen equations in sixteen unknowns and can produce a correction matrix. However, since adjacent pixels in a scene are rarely the same, the SOC calibration cannot produce fully-corrected output hyperspectral data cubes that have high fidelity with the scene. For this reason, it was necessary to gain further understanding of this camera system and its impact upon our SASD algorithms to locate anomalous sources in a scene.

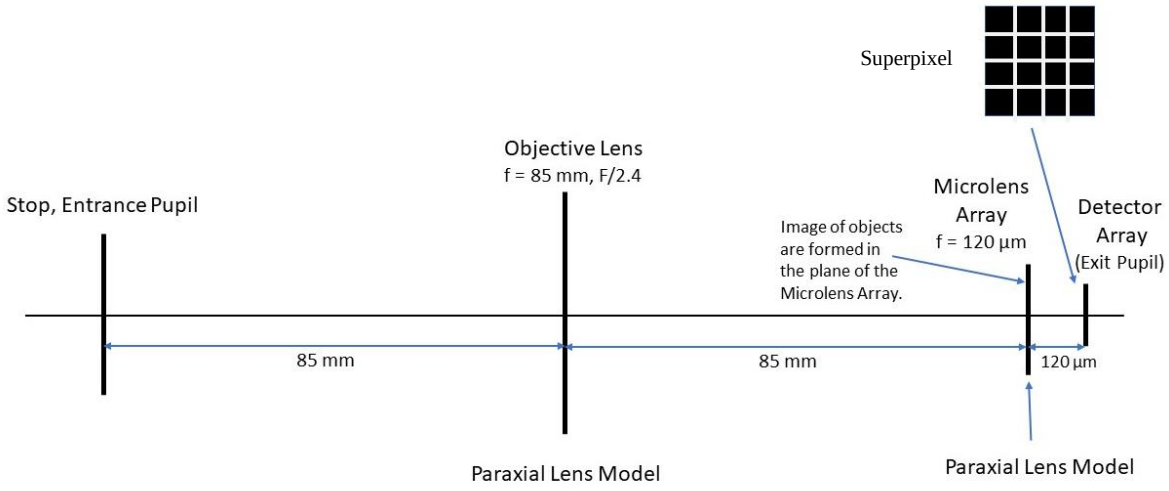


Figure 5. Optical configuration of an ideal telecentric phenoptic camera.

To achieve the desired understanding, a simulation was constructed of a telecentric phenoptic camera having the basic characteristics of the SOC716. Because the actual lens design for the SOC716 was not available, paraxial or ideal lenses were used since this would provide the best performance such a camera could achieve by being a diffraction-limited simulation. Using the actual filters, objective lens, and microlens array can only degrade the performance as a result of any aberrations, component fabrication and alignment errors, ghosting, etc. that might exist. The optical configuration of an ideal telecentric phenoptic camera is illustrated in Figure 5. The spectral filter array, which is located at the front focal plane of the objective lens, becomes the aperture stop of the system. Locating the stop at this location is the necessary condition to achieve telecentric behavior of the objective lens.

The ideal telecentric phenoptic camera shown in Figure 5 functions in the following manner. Light from the scene is incident upon the spectral filter array and is separated into sixteen spectral "channels" or paths. The area or region in the scene (scene pixel) corresponding to a superpixel is

[7] Section 4. of footnote 2.

imaged by the objective lens at the microlens array (MLA). At this point, the optical flux from the scene pixel has been separated into sixteen F/16.2 optical paths and are mingled together. In order to detect the flux from each spectral band from the scene pixel, the MLA reimages the spectral filter array onto the sixteen detectors comprising the superpixel. Since the spectral filter array is located at the front focal plane of the objective lens, any point on this array can be considered to be collimated by the objective lens. These collimated beams are then refocused by the MLA onto the detectors comprising the superpixels which separates the beams. The pixel size used in the SOC716 is 7.4 µm by 7.4 µm. As shown in Figure 4, the focal length of the microlenses is 120 µm. The size of each filter in the spectral filter array is therefore 7.4 µm by 7.4 µm times the pupil magnification (85 mm / 120 µm = 708) or 5.25 mm by 5.25 mm. Figure 6 depicts the spectral filter array and shows the filter locations that SOC selected, as well as the location of the optical axis of the objective lens.

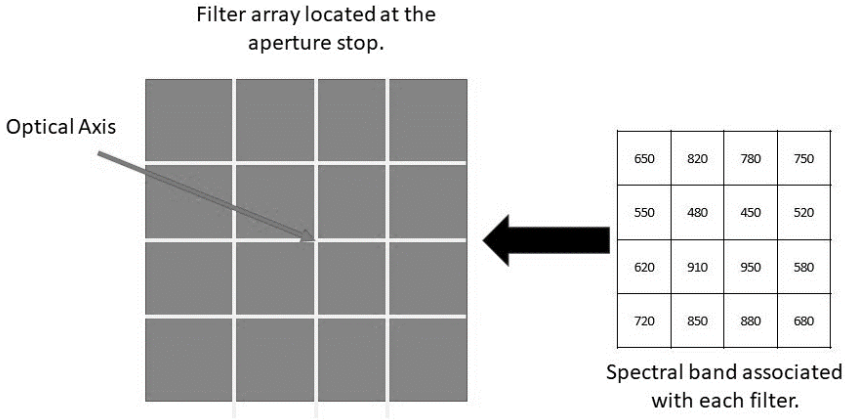


Figure 6. Layout of spectral filter array located at the stop of the objective lens. The unit of the spectral band associated with each filter is nm.

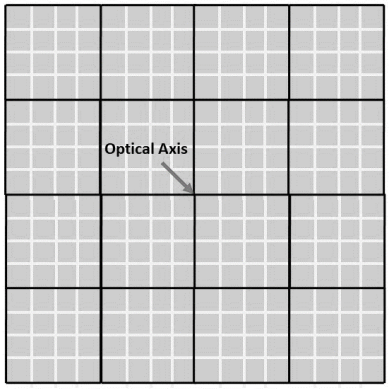


Figure 7. Portion of the CCD showing the optical axis and the relationship between detectors (light blue) and superpixels (black boundaries).

For the purpose of simulating an ideal telecentric phenoptic camera, it is assumed that the fill factor of the CCD is 100%. Figure 7 shows the central part of the CCD 512x512 superpixel array as a 4x4 pixel array of superpixels. The sixteen detectors located in each superpixel are also depicted along with the optical axis of the system. In the simulation, perfect alignment of the spectral filter array, objective lens, MLA, and CCD were assumed. As will be illustrated in the following

analysis, a PSF centered on its corresponding detector in a superpixel likely will not only spill flux onto other detectors in its superpixel, but in some cases onto detectors in adjacent superpixels.

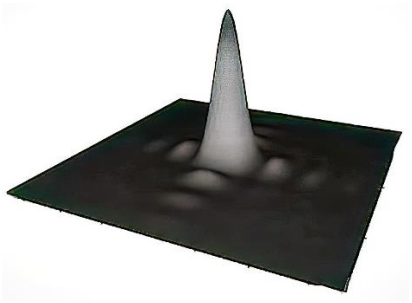

Figure 8. Impulse response at detector plane for λ = 520 nm.
The length of the sides of the illustration are 70 μm.

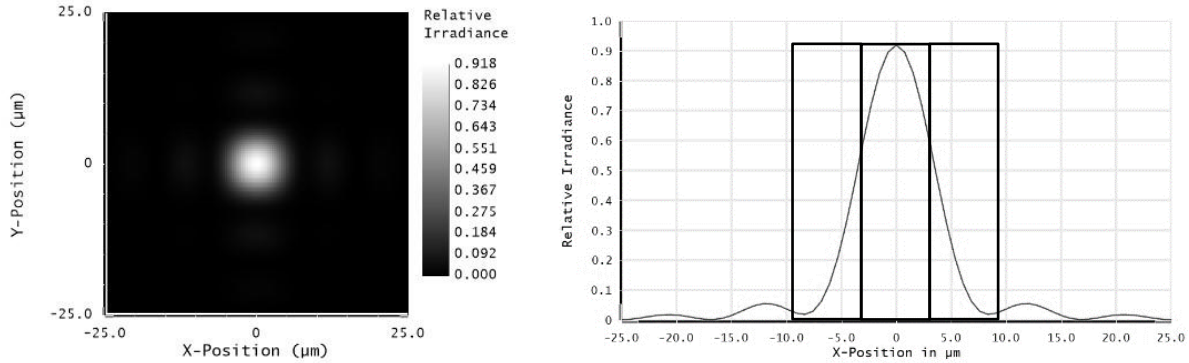


Figure 9. Relative irradiance image of the PSF for λ = 520 nm is shown in the left-side image and a cross-section through the center of the PSF is shown on the right-side.

The optical configuration shown in Figure 3 was represented in Figure 5 as a paraxial system free of all alignment errors and optical aberrations other than diffraction. The system shown in Figure 5 was modeled in Zemax OpticStudio 16 to determine the spatial distribution of the diffracted flux at the CCD detectors. A single filter, centered on the optical axis, was modeled as a 5.25 mm by 5.25 mm square aperture. A plane wave (point source located at infinity) was incident on this square aperture. The resulting impulse response (point spread function, PSF) is presented in Figure 8.[8] The side lobes of the PSF are clearly observable and are typical of the diffraction pattern of a square aperture. Figure 9 shows the relative irradiance of the PSF and its cross-section. The three rectangular boxes depict a detector centered on the PSF and two adjacent detectors. As can be seen, the spillage or contamination of the adjacent detectors is significant and non-trivially impacts detectors up to three detectors away from the primary detector. Since this ideal model is limited only by diffraction, the PSF for other wavelengths is found by simply scaling the spatial flux distribution. In other words, the PSF shown in Figure 8 will be spatially smaller for λ = 450 nm

[8] The radius of the first zero for the PSF using a circular aperture is given by 1.22λf/D = 1.22λF/# where D is the aperture diameter and f is the lens focal length. For a square aperture, such as for the filters, the distance from the PSF peak to the first zero is given by λf/D = λF/# measured in the directions of the sides of the filter and D is the length of the side of the square. For this case, the first zero is 0.52 μm * 16.2 = 8.4 μm. Figure 9 is in agreement with this calculation although the first zero is not reached since the PSF shown is defocused by 120 μm which results in some energy being present at the 8.4 μm position.

by a factor of 450/520 = 0.865, or spatially larger for $\lambda$ = 910 nm by a factor of 910/520 = 1.75. The PSF for this system varies in size by a factor of 910/450 or about 2:1. Clearly, this can complicate the data interpretation of the hyperspectral data cubes produced by the SOC716-VNIR or like systems.

An important element of the simulation is the determination of the set of sixteen transformation functions that are used in the generation of the spectrally contaminated image of the input scene. Formulation of these functions is accomplished by first computing the diffraction-limited PSF for each of the sixteen wavelengths. The Zemax OpticStudio optical design and analysis program was used to compute the spatial irradiance distributions (PSF) by using direct integration of Huygens' wavelets method. Also computed was the Strehl ratio which is the ratio of the peak value of the PSF to the peak value of the diffraction-limited PSF. Since the PSF is slightly defocused on the detector array, the Strehl ratio will be less than unity with the shorter wavelengths being a lower value than for the longer wavelengths. Although it is possible to create the PSFs for all sixteen of the filter wavelengths by scaling the PSF for a reference wavelength of $\lambda_0$, the PSFs were individually generated by OpticStudio such that the PSFs were normalize to have equal total energy (not peak normalize).

The transformation functions for this camera system reside in a 12x12x16 matrix. Figure 10 (a) depicts the top view of a representative transformation matrix that contains nine superpixels (S1–S9) and the sixteen detectors which comprise each superpixel. The spatial relationship of the detectors in a superpixel and the filter wavelengths is shown in Figure 10 (b). Creation of each layer of the transformation matrix is accomplished in the following manner. Each of the PSFs are sequentially incident in superpixel S5 for the corresponding layer. The layers are organized as shown in Figure 10 such that Layer 1 → 650nm, Layer 2 → 820nm, Layer 3 → 780nm, etc. All of the PSFs have the same total energy which allows ease of transforming the scene into a contaminated output image. The first layer (1) of the transformation matrix is for detector S5(1). The PSF for $\lambda$ = 650 nm is centered on this detector and the fractional energy incident thereon and on proximate detectors is computed. Figure 11 (b) presents the distribution of energy at S5(1) and over the detectors surrounding S5(1). It is evident that energy is incident on some detectors in superpixels S1, S2, S4, and S5. Figure 12 illustrates the detectors that are receiving $\lambda$ = 650 nm flux greater than one percent of the total energy in this color. As mentioned previously, the assumed spectrally nonselective sensitivity of the detectors results in measured signal from a detector being the sum of flux intended to be incident on it and all of the spillage of flux from flux of other colors that are directed to detectors surrounding the subject detector. In a like manner, Figures 11 (a), (c), and (d) show the distribution of energy at S5(7), S5(4), and S5(11) and over the detectors surrounding each of them, respectively. In Figure 11 (a), the PSF is centered on the 450 nm detector, S5(7). Examination of this figure shows that signals for the 480, 520, 780, and 950 nm are corrupted by over 7% each of the total energy intended for S5(7). Consequently, if the scene contained a single pixel-size 450 nm source, four peak-normalized output signals would be observed, viz., 450 nm → 100%, 480 nm → 11%, 520 nm → 11%, 780 nm → 14%, and 950 nm → 14%. Should the source pixel contain energy at other wavelengths, the spectral contamination of the output signals increases and further increases due to contamination from adjacent superpixels. Traditional spectrographic interpretation would be challenging at best.

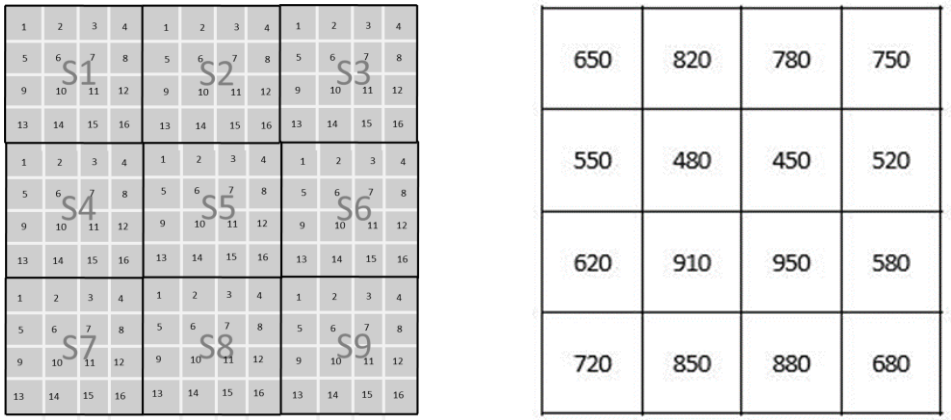


(a) (b)

Figure 10. (a) 3x3 superpixel array with 16 detectors per superpixel (black outlined boxes). (b) The detectors in each superpixel are assigned wavelengths as indicated with the wavelength unit being nm.

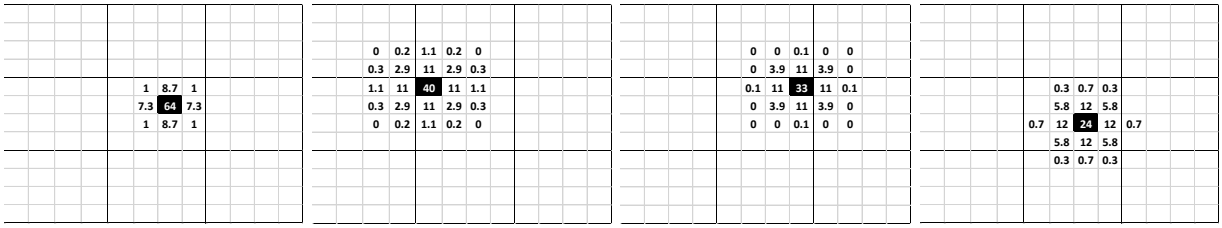


(a) (b) (c) (d)

Figure 11. Representative relative spectral signals from diffraction-limited point spread functions for spectral bands of (a) 450 nm, (b) 650 nm, (c) 750 nm, and (d) 950 nm. The detector corresponding to the specified wavelength is designated by the black detector with white numerals. The thick black boarders identify the superpixels and the 16 detectors in each superpixel are bounded by the light gray lines. Values shown are percentage of total energy.

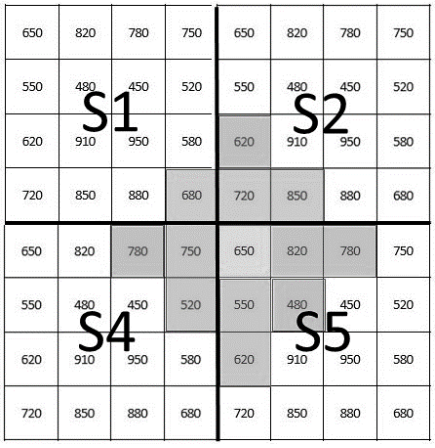


Figure 12. Detectors that are receiving $\lambda$ = 650 nm flux greater than one percent of the total energy in this color are shown where the PSF is centered on S5(1). The numbers in the detector locations are the wavelengths in nm associated with that detector.

Table 1. ODC contamination for flux from OS(i, j, 1) = 500 μW/cm$^2$. Units of wavelength are nm.

| Layer (λ) | ODC(i, j) | ODC(i-1, j) | ODC(i-1, j-1) | ODC(i, j-1) |
|---|---|---|---|---|
| 1 (650) | 200 | | | |
| 2 (820) | 55 | | | |
| 3 (780) | 5.5 | | | 5.5 |
| 4 (750) | | | | 55 |
| 5 (550) | 55 | | | |
| 6 (480) | 14.5 | | | |
| 7 (450) | 1.5 | | | 1.5 |
| 8 (520) | | | | 14.5 |
| 9 (620) | 5.5 | 5.5 | | |
| 10 (910) | 1 | 1 | | |
| 11 (950) | | | | |
| 12 (580) | | | 1 | 1 |
| 13 (720) | | 55 | | |
| 14 (850) | | 14.5 | | |
| 15 (880) | | 1.5 | 1.5 | |
| 16 (680) | | | 14.5 | |

The Output Data Cube (ODC) represents the spectrally corrupted image of the object scene. The ODC is generated by associating each pixel in the object scene (OS) with the corresponding pixel in the ODC using the transformation matrix (TM) with S5 coincident with the imaged pixel. Populating the ODC with spectrally corrupted data can be viewed as a pixel by pixel process; however, since the process is strictly additive, full parallel processing can be performed to reduce the processing time dramatically. Recalling that each object scene pixel comprises sixteen values, each value is fractionally distributed to a multitude of locations in the ODC. For example, consider superpixel ODC(i, j, k) that matches object scene pixel OS(i, j, k) where k designates the layer number. The primary detector in the first layer is designated as number 1 (λ = 650 nm). Referring to Figure 11 (b) and assuming the ideal irradiance of OS(i, j, 1) at ODC(i, j, 1) is 500 μW/cm$^2$, then the distribution of the flux in the ODC is shown in Table 1 illustrating the significant spectral contamination. Similar ODC tables can be generated for each OS(i, j, k). Once the tables are generated, the values in the layer are summed. It is evident that flux from ODC(i, j, k) causes spectral contamination in not only its own superpixel, but in the surrounding eight superpixels. In a like manner, each of the surrounding superpixels will also spectrally contaminate ODC(i, j). Consequently, each ODC(i, j, k) can have up to nine values to sum before the final ODC is complete. Equation (1) provides the mathematical representation of this computation where $\mathrm{OS}(i,j,k) = [{}_1a_{i,j}, {}_2a_{i,j}, {}_3a_{i,j}, ..., {}_{16}a_{i,j}]$ and TM is the array of $b$ terms where ${}_k$S1 = ${}_kb_{-1,-1}$, ${}_k$S2 = ${}_kb_{-1,0}$, …, ${}_k$S5 = ${}_kb_{0,0}$, …, ${}_k$S9 = ${}_kb_{1,1}$.

$$\begin{aligned}\mathrm{ODC}(i,j,k) = {}&{}_k a_{i,j} \cdot {}_k b_{0,0} + {}_k a_{i-1,j-1} \cdot {}_k b_{1,1} + {}_k a_{i-1,j} \cdot {}_k b_{1,0} \\ &+ {}_k a_{i-1,j+1} \cdot {}_k b_{1,-1} + {}_k a_{i,j-1} \cdot {}_k b_{0,1} + {}_k a_{i+1,j-1} \cdot {}_k b_{-1,1} \\ &+ {}_k a_{i+1,j-1} \cdot {}_k b_{-1,1} + {}_k a_{i+1,j} \cdot {}_k b_{-1,0} + {}_k a_{i+1,j+1} \cdot {}_k b_{-1,-1}\end{aligned} \quad (1)$$

Generation of the spectrally corrupted image of any object scene can be readily accomplished using Eq. (1), and very rapidly if parallel processing is used. In the next section, the impact of spectral corruption upon the POD and FAR performance to locate anomalous sources is investigated.

## 4. Analysis and Simulation

**4.1. Introduction.** During the final year of the Grant, a new effective computationally-efficient and mathematically-elegant algorithmic method for detection of anomalous sources in hyperspectral imagery was developed where no a priori knowledge of both the anomalous sources and the hyperspectral image is known. The algorithm is based on the assessment of the spectral content of each pixel of the hyperspectral image (HSI) in the context of the spectra of the spatial neighborhood of the pixel, i.e., the surrounding proximate pixels. The Heidary-Johnson detection process developed previously determined the incongruence of each pixel.[1] Although it yielded impressive performance, the requirement for the user to select a subset of the hyperspectral bands comprising the image and an incongruence threshold made the process somewhat difficult to use in near real-time applications. On the other hand, the new detection method is essentially autonomous, provides excellent performance, and appears to be amenable for real-time applications and implementation in hardware. In the next subsection the methodology is presented and in Subsection 4.3, an analysis of the method is presented using several examples. Included is a comparison of the original HSI and the image when spectrally blurred/corrupted by the telecentric phenoptic hyperspectral camera discussed above. The method is utilized in Subsection 4.4 to determine the probability of detection (POD) and false alarm rate (FAR) of a variety of anomalous sources in different hyperspectral images. This analysis demonstrates the algorithm's impressive performance in accurately locating anomalous sources while rarely misclassifying a pixel as anomalous.

**4.2. Methodology.** In this investigation, the anomalous source is assumed to be contained totally within a single pixel. The contamination factor (*a*) of a pixel in an existing image by an anomalous source being evaluated can range from 0% to 100%. In the anomalous source detection analysis in Subsection 4.4, an anomalous-source contaminated pixel is constructed to be arguably the most stressing case by making the total energy in the contaminated pixel (*cp*) equal to the total energy in the original pixel (*op*). To accomplish this, a normalizing factor $\Re$, the ratio of the total energy in the original pixel to the total energy of the anomalous source (*as*), is used. The energy in each spectral band is given by

$$ {}_{cp}E(\lambda) = a\Re({}_{as}E(\lambda)) + (1-a)({}_{op}E(\lambda)) \tag{2} $$

where $\int {}_{cp}E(\lambda)d\lambda = \int {}_{op}E(\lambda)d\lambda$ for $a = 0$ to 1; however, the spectral values of ${}_{cp}E(\lambda)$ may be significantly greater or smaller than the corresponding values of ${}_{op}E(\lambda)$. Using Eq. (2) to create a contaminated pixel (i) minimizes the possibility that the pixel will appear brighter or dimmer than the original pixel and (ii) maximally stresses the detection algorithm performance.

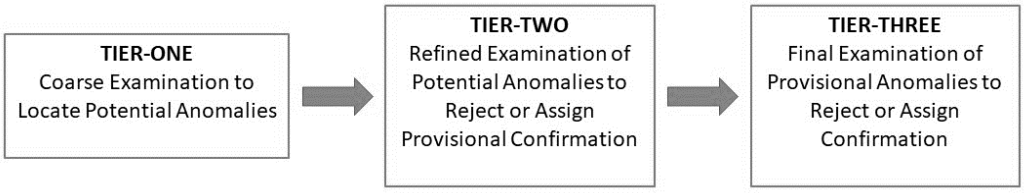


Figure 13. Three tier process to identify potential anomalous sources.

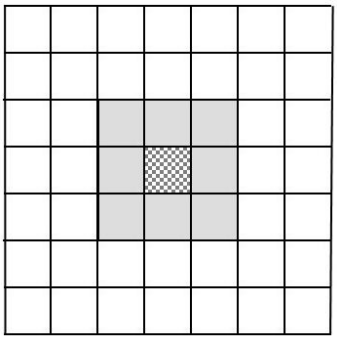

Figure 14. A portion of the input hyperspectral image is shown with the "core" pixel under examination being designated by the checkered pattern and the surrounding eight pixels shown in gray. These eight pixels are called a "pixel ring." The 3x3 pixel block is denoted as a "kernel."

The anomaly detection process of a contaminated input hyperspectral image comprises three separate steps or tiers as illustrated in Figure 13. Tier-1 exams all of the pixels in the HSI where the characteristics of the pixel and the eight surrounding pixels, illustrated in Figure 14, are compared using a method explained below. The disparity of the pixel with respect to its neighbors provides a metric to provide a coarse identification of *potential* anomalous sources in which each has typically different radiant and spectral characteristics. Tier-1 dramatically decreases the number of pixels that require a more refined examination. These potential anomalous source pixels are analyzed by the Tier-2 process that more rigorously determines if a suspect pixel should be provisionally designated as an anomalous source. The number of candidate anomalous pixels is further reduced by Tier-2 for the final Tier-3 analysis. The provisional anomalous pixels are meticulously analyzed in Tier-3 by examination of the spectral relationship between all of the pixels in the 3x3 ring of pixel about the subject pixel. Those pixels selected by the Tier-3 process are then designated as anomalous pixels. The computational load per pixel increases by Tier, but the number of pixels examined markedly decreases by Tier which makes it reasonable to anticipate that real-time analysis of a video stream can be realized using current hardware. For example, consider a hypothetical hyperspectral image that contains 1,500,000 pixels with 100 actual anomalous sources scattered throughout the image. The Tier-1 process might identify say 20,000 candidate pixels, Tier-2 reduces the number to perhaps 1,200, and then Tier-3 identifies perhaps 101 pixels where 99 pixels containing an anomalous source are found, one is missed, and two pixels are misclassified (false positive or false alarm). Subsection 4.4 presents actual examples.

**4.2.1. Process Summary.** The anomaly detection process is summarized in this subsection and the mathematical formulation of the three-tier method is presented in Subsection 4.2.2.

- The image data cube comprises $Q$ spectral bands/channels with the image dimensions being $M$ by $N$ pixels. Data cube size is $M$x$N$x$Q$. The value of each pixel is the intensity I(m,n) [9] .

- A datum kernel is defined as a 3x3 by $Q$ portion of the image where the center/core pixel of the data kernels are the pixels in which anomalous sources may exist.

- **Tier-1**: The data kernels comprising the entire image are examined. The total number of the data kernels is ($M$-2)x($N$-2).
    - The mean intensity value of each datum kernel pixel ring is computed for each spectral band. This data cube has dimensions of ($M$-2)x($N$-2)x$Q$.
    - The value of each (i) kernel core intensity and (ii) kernel mean intensity are normalized. The resultant data cube has dimensions for each of ($M$-2)x($N$-2)x$Q$.
    - Spectral compression is accomplished by creating a Hyperspace Angle Map (HAM) image, for each kernel core pixel, computing the angle between the spectrum of the normalized core pixel intensities and the kernel mean intensities, i.e., the inverse cosine of the inner product for each core pixel. The resultant HAM data cube has dimensions of ($M$-2)x($N$-2), and a compression factor of Q.
    - The HAM image is evaluated to located pixels where anomalous sources may be situated. The HAM image pixels having an angle greater than a user-specified threshold angle, e.g., 4–6°, comprise the Tier-1 set $\{P\}$ of candidate pixels that contains $p$ = n($P$) locations.

- **Tier-2**: The number of candidate pixels are further significantly decreased by refining the threshold to identify those kernels to be analyzed by the Tier-3 process.
    - The mean-HAM, $\bar{A}$, for each candidate kernel is computed by taking the mean value of the HAM kernel ring. This results in $p$ values of $\bar{A}$.
    - The standard deviation of each HAM kernel ring, $A_\sigma$, is computed next. This results in $p$ values of $A_\sigma$.
    - A new threshold angle is established with the value of $\beta = [\bar{A} + \kappa A_\sigma]$ where $\kappa$ is a scaling factor, typically 1 to 2.
    - The $p$ HAM kernels comprising $\{P\}$ determined in Tier-1 are evaluated to locate pixels having a HAM angle greater than the threshold angle $\beta$. This results in a set $\{R\}$ comprising $r$ pixel locations where $r$ = n($R$) << n($P$) and $R \subseteq P$.
    - The resultant pixel locations in $\{P\}$ have been further reduced to $\{R\}$ for Tier-3 examination.

- **Tier-3**: Final identification of potential anomalous sources is determined by utilizing the spectrally expanded normalized intensity data for the $R$ pixel kernels to create further a refined anomaly detection threshold.
    - For each of the $r$ pixel kernels, the i$^{th}$ angle $A_i$, between the kernel ring mean and each of the eight ring pixels are computed.

[9] Intensity of a pixel in this context means the digital value of a pixel in both a hyperspectral image (HSI) and a HAM image with the former being relatable to radiometric quantities and the latter to angular quantities.

- The mean value, $\bar{A}$, of these eight $A$'s and the related standard deviation, $A_\sigma$, are computed.
- A new threshold angle is established with the value of $\gamma = [\,\bar{A} + \chi A_\sigma\,]$ where $\chi$ is a scaling factor, typically 1 to 2.
- A set $\{S\}$ comprising $s$ pixels is formed from the set of $r$ pixels where the HAM angle between the kernel core and the kernel ring mean is greater than the threshold angle $\gamma$.
- The $\{S\}$ provides the pixel locations of probable anomalous sources where n($S$) << n($R$) and $S \subseteq R$.

- The likelihood of the rank ordering of elements comprising sets $\{P\}$, $\{R\}$, and $\{S\}$ being the same is remote; however, it is relatively improbable, but possible, that anomalous pixels in $\{P\}$ and $\{R\}$ will not be contained in $\{S\}$.

- It is noted that the search for anomalous pixels could be started by applying the procedure of Tier-3 to the entire image; however, the computational resources would be incredibly huge compared to using the Tier-1, Tier-2, and Tier-3 process that progressively decreases the computational effort.

**4.2.2. Mathematical Formulation of Three-Tier Process.** The anomaly detection process of the input hyperspectral image begins by computing the mean-HSI (MHSI) intensity which has the same spatial and spectral dimensions as the input HSI. The value assigned to each pixel in a spectral band of the MHSI is obtained by computing the spatial correlation of the respective pixel in the input HSI with its surrounding 3x3 pixel ring, viz.,

$$\bar{\mathrm{I}}(m,n,\mathrm{q}) = \frac{1}{8}\left[\sum_{j=-1}^{1}\sum_{i=-1}^{1}\mathrm{I}\big((m+i),(n+j),\mathrm{q}\big) - \mathrm{I}(m,n,\mathrm{q})\right]; \quad 1 \le m \le M, 1 \le n \le N, 1 \le q \le Q \qquad (3)$$

where, $\mathrm{I}$ and $\bar{\mathrm{I}}$ represent, respectively, the input HSI and the corresponding MHSI, and $M, N,$ and $Q$ denote the spatial dimensions and the number of spectral bands, respectively. Both the HSI and the MHSI images are normalized as shown in Eq. (4).

$$\hat{\mathrm{I}}(m,n,\mathrm{q}) = \frac{\mathrm{I}(m,n,q)}{\sqrt{\sum_{q=1}^{Q}\mathrm{I}^2(m,n,q)}}, \quad \hat{\bar{\mathrm{I}}}(m,n,\mathrm{q}) = \frac{\bar{\mathrm{I}}(m,n,q)}{\sqrt{\sum_{q=1}^{Q}\bar{\mathrm{I}}^2(m,n,q)}} \qquad (4)$$

where $\hat{\mathrm{I}}$ and $\hat{\bar{\mathrm{I}}}$ denote the normalized HSI and MHSI, respectively.

The next step in the anomaly detection process maps the normalized three-dimensional hyperspectral image and mean-hyperspectral image into a two-dimensional (2D) intensity image called Hyperspace Angle Mapping (HAM). The intensity value of each pixel in the HAM image represents the angle between the spectrum of the corresponding pixel of the HSI and the mean

spectrum associated with the eight-pixel ring surrounding the pixel under consideration.[10] Specifically, the HAM image is obtained by computing the pixel-wise inner product of the normalized HSI and MHSI and taking the inverse cosine of each the inner product at each pixel as given by Eq. (5).

$$\mathrm{A}(m,n) = \frac{180}{\pi}\cos^{-1}\left(\sum_{q=1}^{Q}\hat{\mathrm{I}}(m,n,q)\,\hat{\bar{\mathrm{I}}}(m,n,q)\right); \quad 1 \le m \le M,\ 1 \le n \le N \tag{5}$$

where $\mathrm{A}(m,n)$ is the HAM image transformation of the input HSI and provides a 2D intensity (grayscale) image[11] wherein the value of each pixel represents the angle between the spectra of the normalized HSI and the MHSI at the corresponding pixels.

As illustrated in Figure 13, the first tier (Tier-1) of the hyperspectral anomaly detection system examines the HAM image in order to flag a relatively small subset of pixels as candidates for further examination by higher tiers. In Tier-1, the intensity of the 2D HAM image pixels are (i) compared to a user-prescribed angle-threshold and (ii) the $\mathrm{A}(m,n)$ pixels whose intensities are greater than angle-threshold are flagged as potential anomalies while the other pixels are eliminated from the suspected anomaly candidate list $\{P\}$. Examination of a variety of images indicates that the Tier-1 angle-threshold lies in the range of 4–6 degrees.

The mean-HAM image $\bar{\mathrm{A}}$ is computed, as shown in Eq. (6), by taking the correlation of the HAM image A with the 3x3 pixel ring about each HAM pixel core. The standard deviation HAM image $\mathrm{A}_\sigma$ is created using Eq. (7) where each pixel in the image expresses the standard deviation of the elements of the pixel ring about its corresponding HAM image pixel core, with respect to the $\bar{\mathrm{A}}$ of the pixel ring.

$$\bar{\mathrm{A}}(m,n) = \frac{1}{8}\left[\sum_{j=-1}^{1}\sum_{i=-1}^{1} A\big((m+i),(n+j)\big) - A(m,n)\right] \tag{6}$$

$$\mathrm{A}_\sigma(m,n) = \sqrt{\frac{1}{8}\left(\sum_{j=-1}^{1}\sum_{i=-1}^{1}\left[\mathrm{A}((m+i),(n+j)) - \bar{\mathrm{A}}(m,n)\right]^2 - \left[\mathrm{A}(m,n) - \bar{\mathrm{A}}(m,n)\right]^2\right)} \tag{7}$$

All the pixel locations in $\{P\}$ which pass the Tier-1 detection criterion are examined by the Tier-2 process. The Tier-1 pixels in $\{P\}$ for which HAM angles exceed $\bar{\mathrm{A}}$ plus $\kappa$ times $\mathrm{A}_\sigma$ are designated by the Tier-2 process for further scrutiny by the Tier-3 process. These Tier-2 pixels constitute set $\{R\}$ where $\mathrm{n}(R) << \mathrm{n}(P)$ and $R \subseteq P$.

As explained in 4.2.1, Tier-3 utilizes a more sophisticated method to locate candidate anomalous pixels. In Tier-3, a second Hyperspace Angle Map, denoted by *A* rather than by A as in Tier-2, is computed, using Eq. (8), where the angles between the kernel ring mean and *each* of the eight ring

[10] The hyperspace angle map concept was introduced in the 2017 Interim Report associated with location of an anomalous source that is partially positioned in two, three, or four adjacent pixels.
[11] This image is spectrally compressed, i.e., the spectral information for each pixel is combined into a single value.

pixels are determined for each of the *r* pixel kernels. The values of $\hat{\mathrm{I}}$ and $\hat{\bar{\mathrm{I}}}$ were previously computed in Tier-1 using Eq. (4).

$$A(m+i,n+j)=\frac{180}{\pi}\cos^{-1}\left(\sum_{q=1}^{Q}\hat{\mathrm{I}}(m+i,n+j,q)\,\hat{\bar{\mathrm{I}}}(m,n,q)\right);\quad -1\le i\le 1,\ -1\le j\le 1;\ \{R\} \tag{8}$$

The Tier-3 $\bar{A}$ is the mean value of the eight *A* values for each kernel ring as computed using Eq. (9).

$$\bar{A}(m,n)=\frac{1}{8}\left[\sum_{j=-1}^{1}\sum_{i=-1}^{1}A\big((m+i),(n+j)\big)-A(m,n)\right] \tag{9}$$

Equation (10) is used to determine the standard deviation, $A_\sigma$, of *A* of the eight pixels comprising the kernel ring with respect to its $\bar{A}$.

$$A_\sigma(m,n)=\sqrt{\frac{1}{8}\left(\sum_{j=-1}^{1}\sum_{i=-1}^{1}\left[A((m+i),(n+j))-\bar{A}(m,n)\right]^2-\left[A(m,n)-\bar{A}(m,n)\right]^2\right)} \tag{10}$$

Similar to Tier-2 anomaly detection, a Tier-3 threshold angle for each kernel is given by

$$\gamma=[\,\bar{A}+\chi A_\sigma\,] \tag{11}$$

where $\chi$ is a scaling factor, typically 1 to 2. A set $\{S\}$ comprising *s* pixels is formed from the set of *r* pixels where the angle between the kernel core $A(m,n)$ and the kernel ring mean $\bar{A}(m,n)$ is greater than the threshold angle $\gamma$. This process to identify probable anomalous sources typically reduces the size of the Tier-2 set $\{R\}$ considerably. The resultant set $\{S\}$ provides the pixel locations of probable anomalous sources where n(*S*) << n(*R*) and $S\subseteq R$. The elements of $\{S\}$ can be rank ordered by the extent the angle is greater than the threshold angle $\gamma$. In general, those pixels having the greatest angle above $\gamma$ are those most likely to contain a subpixel-scale anomalous source.

**4.3. Analysis.** Several multispectral images obtained from the Manchester University multispectral database[12] were used to evaluate the performance of the subpixel-scale anomalous source detection process. These are designated as Scene-5, Scene-6, and Scene-7. Another scene was used to create a variety of hyperspectral anomalies. As will be presented, the three-tier process performs remarkably well and arguably superior to the authors' original process.[1] An important question addressed in this section is what is the impact of spectral corruption of the image in locating anomalous sources. Since the algorithms for the three-tier process have no a priori

[12] https://personalpages.manchester.ac.uk/staff/d.h.foster/Hyperspectral_images_of_natural_scenes_04.html. The intensity response at each pixel, recorded with 12-bit precision, was linear over the entire dynamic range. The peak-transmission wavelength was varied over 400–720 nm with bandwidth (full width at half maximum) of 10 nm at 550 nm, decreasing to 7 nm at 400 nm and increasing to 16 nm at 720 nm.

knowledge of the content of the image and of potential anomalous sources, it is possible that the anomalous source detection of a spectrally corrupted image could be worse, the same, or better than without the corruption. Subsection 4.4 explores an answer to this question.

**4.3.1. Performance using a Spectrally Non-Corrupting Camera.** In this case, the image hyperspectral and spatial data are unchanged when the algorithms are applied. It is of course unknown what spectral corruption of the image was caused by the instrument creating the imagery. For the purpose of this investigation, the Manchester University multispectral database is considered spectrally non-corrupted. The Scene-5 data cube is a thirty-two-band high-resolution image with 1020x1339 pixels; its RGB rendition is shown in Figure 14. The first band of this data cube was eliminated due to its noisy behavior and the remaining 31-band data cube was converted to a 16-band HSI by taking the mean of consecutive pairs of bands. Figure 15 illustrates a grayscale representation of the resultant 16-band Scene-5 data cube, i.e., the data cube was compressed into a single band. Figures 16 and 17 show the HAM image and the $A_\sigma$ image associated with the 16-band Scene-5 image. Figures 18 and 19 show, respectively, the histogram and the cumulative distribution of the HAM angles. It is noted that 99.9% of pixels have HAM angles which are smaller than 10°, and 69.2% of HAM angles are less than 2°.

Figure 20 shows the effects of angle threshold and scaling factor $\kappa$ on the number of flagged potential anomalies. For Tier-1, the abscises angle threshold is user specified while the Tier-2 angle thresholds $\beta$(m,n) are determined for each Tier-1 pixel located at (m,n) using $\beta(m,n) = \bar{A}(m,n) + \kappa A_\sigma(m,n)$. For Tier-1, Figure 20 presents the number of pixels that have a HAM angle greater than the angle threshold shown on the abscissa. In contrast, Tier-2 does not have a single angle threshold as there is for Tier-1 since each Tier-2 pixel has its own unique angle threshold $\beta$(m,n). The Tier-2 plots are interpreted to mean that for any angle threshold shown on the abscissa, the value on the ordinate is the number of pixels passed by Tier-1 that also pass the Tier-2 angle threshold test. Further, as illustrated in Figure 20, a horizontal line from the Tier-2 plots drawn to the intersection with the Tier-1 plot reveals the *minimum* angle threshold value $\beta_{\min}(m,n)$ passed by the Tier-2 process. For example, if 4° is selected as the threshold angle for Tier-1 pixels, then the minimum angle thresholds for Tier-2 pixels are 5° and 5.8° for $\kappa$ = 1.5 and 2, respectively.

For the image shown in Figure 16, setting the angle threshold to 4° results in 56,000 pixels being designated as suspect anomalies by the Tier-1 process. Letting $\kappa$ = 1.5, the Tier-2 anomaly detection process identifies 21,972 pixels or 1.6% of total pixels comprising the image. Likewise, for $\kappa$ = 2, the Tier-2 process selects 11,127 pixels which is 0.8% of total pixels in the image. These Tier-2 designated pixels are further examined by the Tier-3 process. Since there were no anomalies inserted in Figure 16, the Tier-3 process detected zero potential anomalies. Had this image been process by the incongruence method, a number of false-positive pixels would have been declared as anomalies. This behavior of the new method, compared to the incongruence method, is an important improvement in being able to detect "weirdness" in an image. Weirdness of a kernel can be considered a measure of the characteristic dissimilarity between the core pixel and its pixel ring. Interestingly, the Tier-3 process recognizes that the weirdness threshold can vary significantly from kernel to kernel thereby drastically reducing the probability of false-positive declarations being made.

In summary, all of the HSI pixels designated by the Tier-2 process are input to the Tier-3 process. In Tier-3, the spectra of the nine pixels comprising the 3x3-pixel block centered at the flagged pixel are examined as previously explained. The eight angles between the spectra of the eight pixels of the ring and the mean spectrum of this pixel ring are computed, and the mean and the standard deviation of these angles are recorded. If the HAM angle of the center pixel exceeds the above mean angle by more than $\chi$ standard deviations, the examined pixel is declared an anomaly, otherwise it is not.

Figure 14. Color image representation of Scene-5 with dimensions of 1020x1339x32.

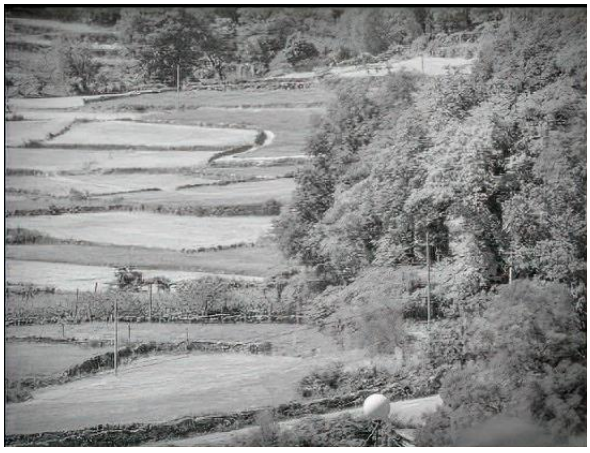

Figure 15. Grayscale image representation of Scene-5 with dimensions of 1020x1339x16.

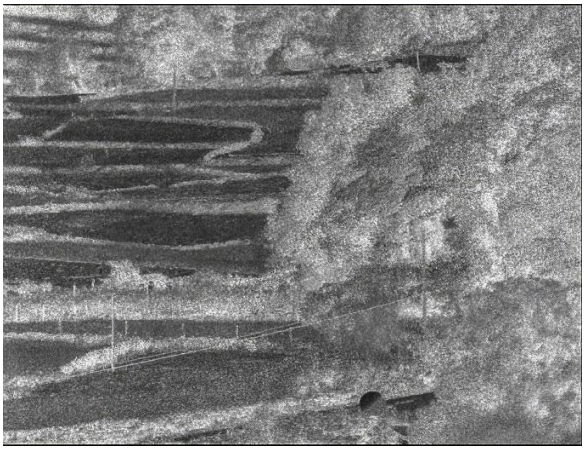

Figure 16. The HAM image of the 16-band Scene-5 image. The greatest HAM angle is 56°.

Figure 17. The $A_\sigma$ image of the 16-band Scene-5 image.

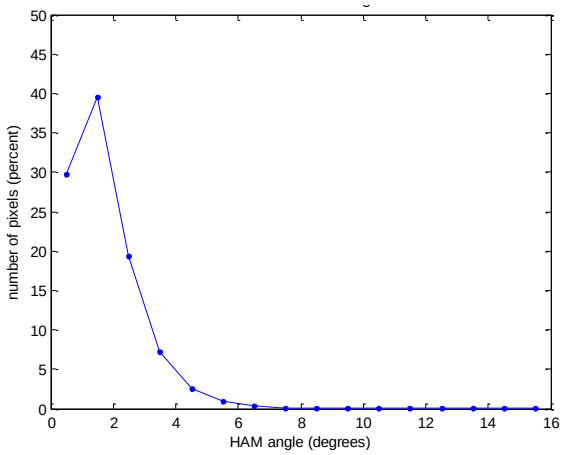


Figure 18. Histogram of HAM angles of the 16-band Scene-5 image. The width of each angle bin is one degree. The centers of the lowest and highest bins are, respectively, at 0.5° and 15.5°. All 602 pixels whose HAM angles are greater than 15° are included in the last bin.

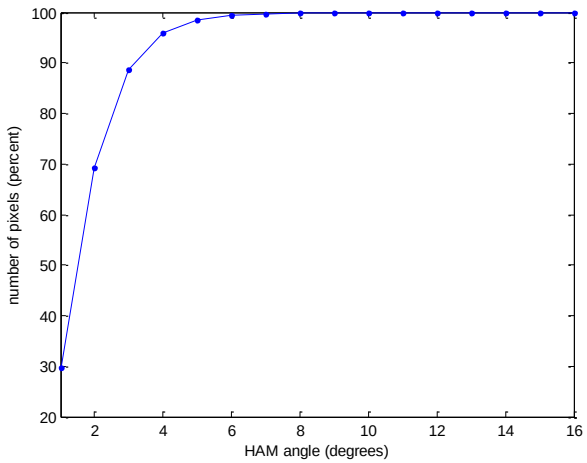


Figure 19. Proportion of HSI pixels whose HAM angles are smaller than the respective values on the abscissa.

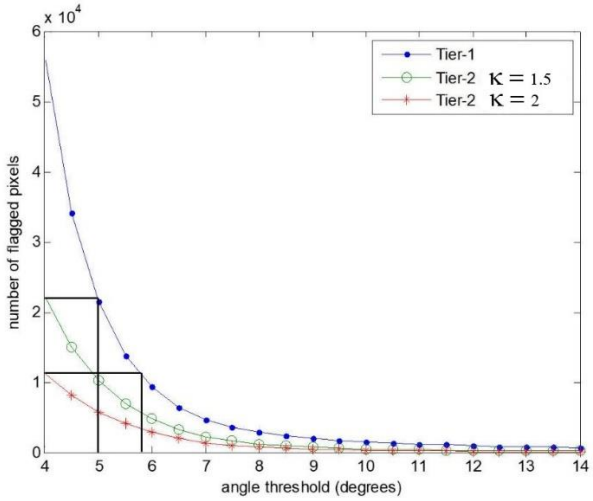


Figure 20. Number of designated pixels in the 16-band image of Scene-5 versus of Tier-1 angle threshold and Tier-2 $\kappa$ value.

Figure 21. RGB rendition of Scene-6 that has a hyperspectral data cube size of 1021x1338x33.

Figure 22. Intensity or grayscale image of Scene-6 after the hyperspectral data cube has been decreased to a size of 1021x1338x16.

Manchester image Scene-6 is a hyperspectral data cube having dimensions of 1021x1338x33 and its RGB rendition is shown in Figure 21. The first band of the original 33-band image was removed due to its excessively noisy nature, and subsequently, the pixel-wise summation of consecutive pairs of bands are assigned to respective bands to create the transformed 16-band HSI. The intensity or grayscale image formed by spectrally compressing the 16-band HSI is presented in Figure 22. Figures 23 and 24 show the HAM and the $A_\sigma$ images for the 16-band HSI. Figures 25 and 26 show, respectively, the histogram and the cumulative distribution of the HAM angles. It is noted that HAM angles for 99.9% of pixels are smaller than 6° and 80.4% of HAM angles are less than 2°. The plots of Figure 27 show the effects of angle threshold and $\kappa$ on the quantity of designated anomalies. It is noted that if the angle threshold is set to 4°, the Tier-1 process determines 7,339 pixels are suspected anomalies, while the Tier-2 process identifies 3,413 and 2,119 pixels for $\kappa$ equal to 1.5 and 2, respectively. The Tier-2 process, setting the threshold angle to 4° and $\kappa$ threshold to 1.5, finds that 0.25% of pixels are designated as candidate anomalies for further examination by the Tier-3 process. As was for Scene-5, no anomalies were inserted in Figure 23 and the Tier-3 process detected zero potential anomalies. It is possible that the Tier-3 process does not detect an anomaly or it may declare a non-anomalous pixel to be anomalous (false positive); however, based upon analysis of a number of images, the probability of detecting an anomaly is very high while it is highly unlikely false positives will be declared.

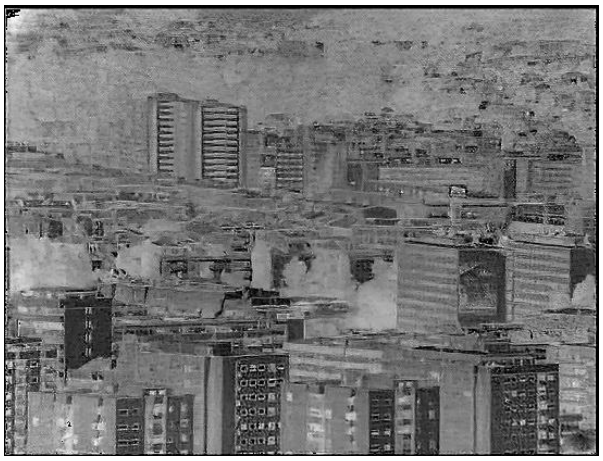

Figure 23. HAM image of the 16-band Scene-6 HSI. The greatest HAM angle is 33.9°.

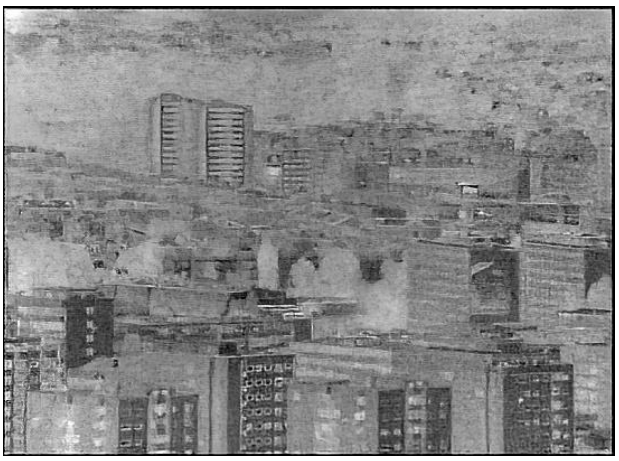

Figure 24. $A_\sigma$ image of the 16-band Scene-6 HSI.

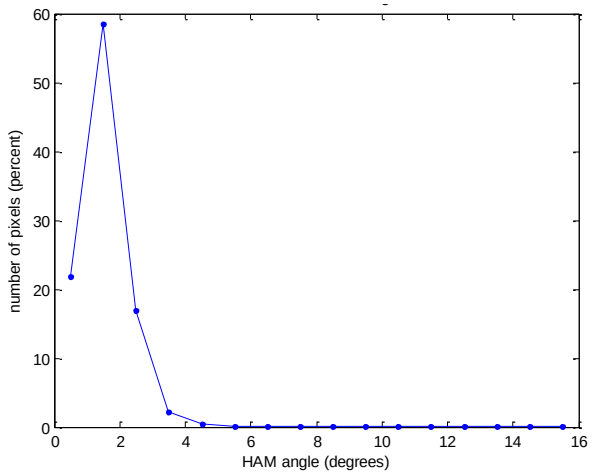


Figure 25. Histogram of HAM angles of the 16-band Scene-6 image. The width of each angle bin is one degree. The centers of the lowest and highest bins are, respectively, at 0.5° and 15.5°. All 149 pixels whose HAM angles are greater than 15° are included in the last bin.

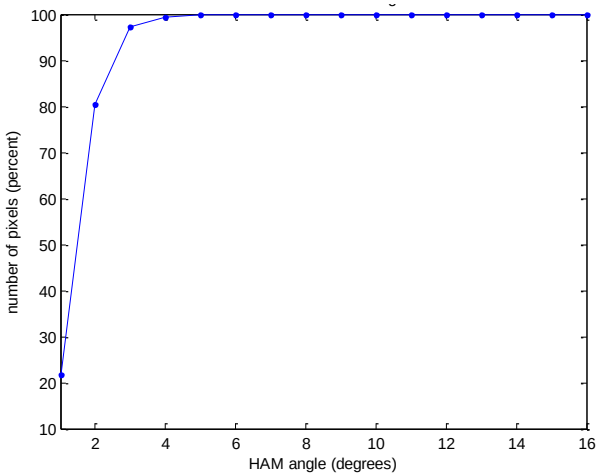


Figure 26. Proportion of HSI pixels whose HAM angles are smaller than the respective values on the abscissa.

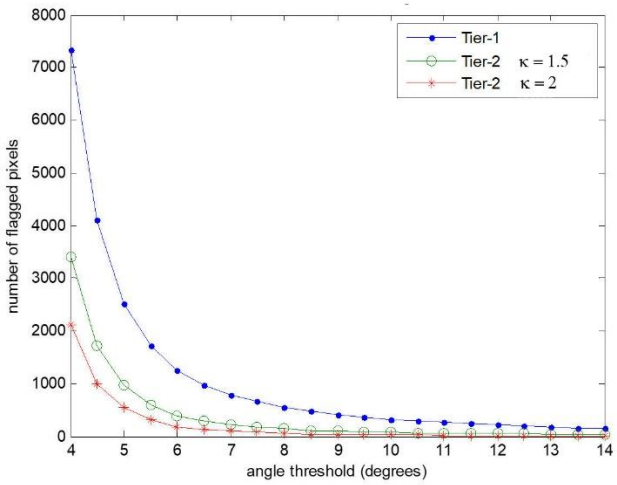


Figure 27. Number of designated pixels in the 16-band image of Scene-6 versus of Tier-1 angle threshold and Tier-2 $\kappa$.

The following images show the RGB rendition of Scene-7 (Figure 28) of the Manchester images, the intensity image obtained by pixel-wise summation of all 16-bands of the transformed HSI (Figure 29), the HAM and the $A_\sigma$ images (Figure 30 and 31). The first band of the original 33-band image is removed due to its excessively noisy nature, and subsequently the pixel-wise summation of consecutive pairs of bands are assigned to respective bands of the 16-band HSI. Figures 32 and 33 show, respectively, the histogram and the cumulative distribution of the HAM angles. It is noted that HAM angles for 99.9% of pixels are smaller than 5°, and 92.4% of HAM angles are less than 2°. The plots of Figure 34 show the effects of angle threshold and $\kappa$ on the number of designated anomalies. It is noted that for a 4° angle threshold, 3,798 pixels are flagged by the Tier-1 process as suspected anomalies, while the Tier-2 process identifies 2,306 and 1,164 pixels for $\kappa$ equal to 1.5 and 2, respectively. Setting the angle and $\kappa$ thresholds at 4° and 1.5, respectively, leads to 0.17% of pixels being selected by the Tier-2 anomaly detection process to be further examined by the Tier-3 process. As for the prior two scenes, Tier-3 detected no anomalies or false positives.

Figure 28. Scene-7 that has a hyperspectral data cube size of 1017x1340x33.

Figure 29. Intensity or grayscale image of Scene-7 after the hyperspectral data cube has been decreased to a size of 1017x1340x16.

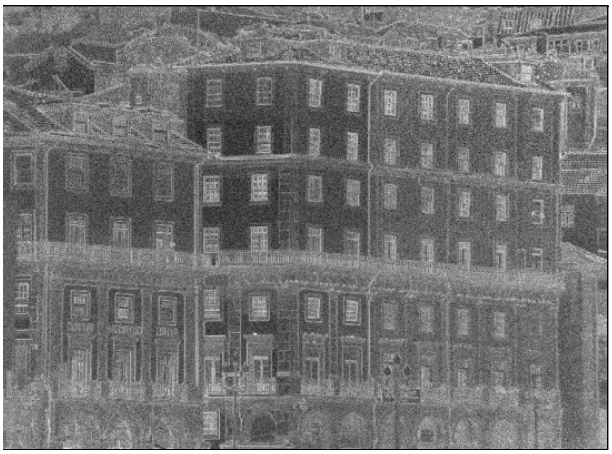

Figure 30. HAM image representation of the 16-band Scene-7 image.

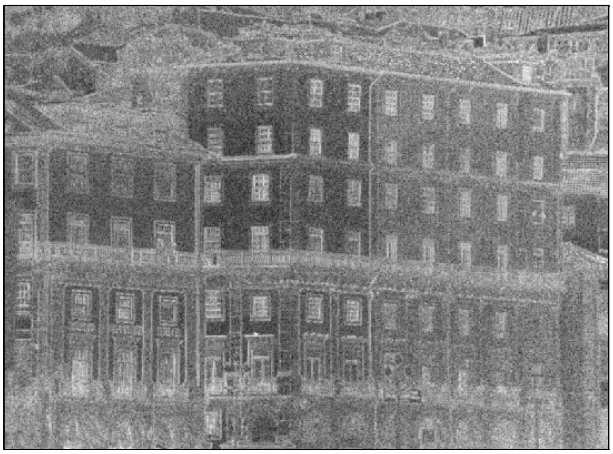

Figure 31. $A_{\sigma}$ image of the 16-band Scene-7 HSI.

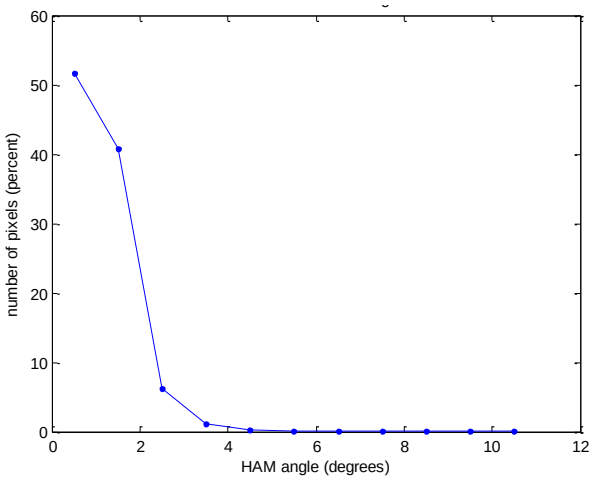


Figure 32. Histogram of HAM angles of the 16-band Scene-7 image. The width of each angle bin is one-degree. The centers of the lowest and highest bins are, respectively, at 0.5 and 10.5°. Maximum HAM angle is 10.17°.

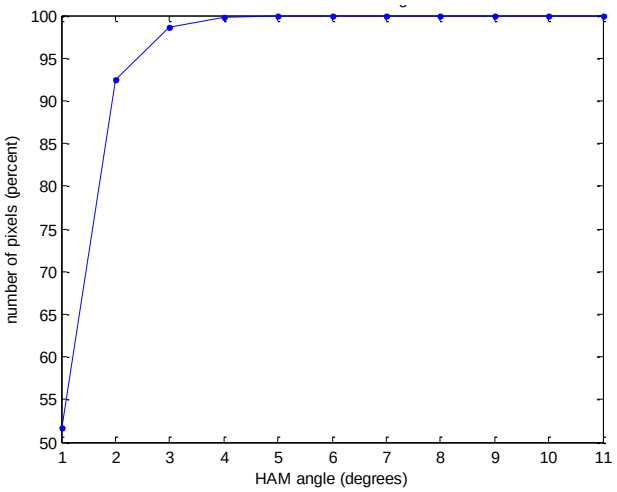


Figure 33. Values on the ordinate show the proportion of HSI pixels whose HAM angles are smaller than the respective HAM angle on the abscissa.

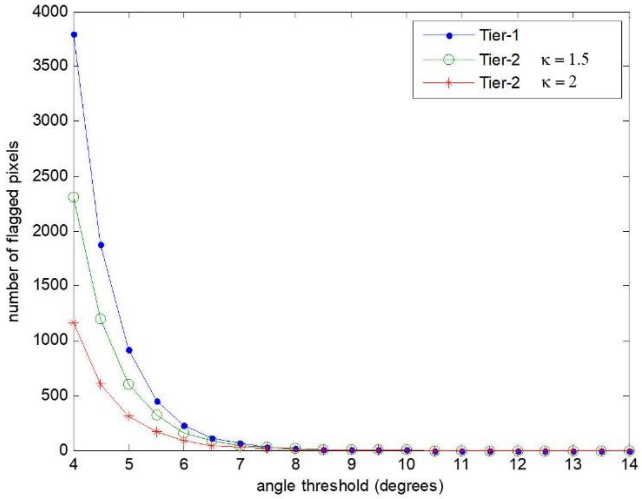


Figure 34. Number of flagged pixels versus of angle-threshold and $\kappa$ for 16-band Scene-7 image.

**4.3.2. Impact of Spectral Blurring/Contamination by Phenoptic Camera.** The spectral-blurring transformation, discussed in Section 3, was applied to the 16-band Scene-5 image in order to synthesize a spectrally-blurred 16-band Scene-5 image. Figure 35 shows the grayscale representation of the spectrally-blurred 16-band Scene-5 image, which was obtained by pixel-wise summation of all the bands. Figures 36 and 37 show the histogram and cumulative distribution of the HAM angles of the spectrally-blurred Scene-5 image compared to the 16-band Scene-5 source image in order to show the effect spectral blurring on the HAM angle distributions. Figure 38 illustrates the effect of spectral blurring on the number of pixels flagged by the Tier-1 and Tier-2 anomaly detection processes. Setting the HAM angle threshold at 4° and $\kappa$ equal to 2, Tier-1 and

Tier-2 designated pixels equal to 55,926 and 11,127, respectively, for the 16-band source image associated with Scene-5, while the number of suspect pixels in the blurred 16-band image are 4,273 and 1,403 pixels, respectively, for Tier-1 and Tier-2. Although a visual comparison of Figures 15 and 35 doesn't show hardly a noticeable difference, Figures 36–38 do illustrate that spectral blurring significantly decreases the range of HAM angles. Tier-3 processing of the Tier-2 spectrally-blurred designated pixels resulted in no false-positive anomalies being detected. The likely reason for this performance is that the Tier-3 process' kernel by kernel threshold determination allows it to adapt to the decrease in kernel weirdness.

Figure 35. Grayscale image of spectrally-blurred 16-band Scene-5 image.

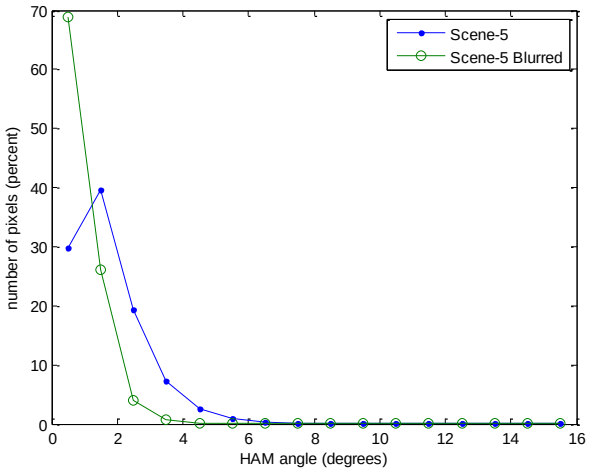


Figure 36. Histograms of HAM angles of the blurred 16-band Scene-5 and original Scene-5 images. The width of each HAM angle bin is 1°. The centers of the lowest and highest bins are, respectively, at 0.5° and 15.5°.

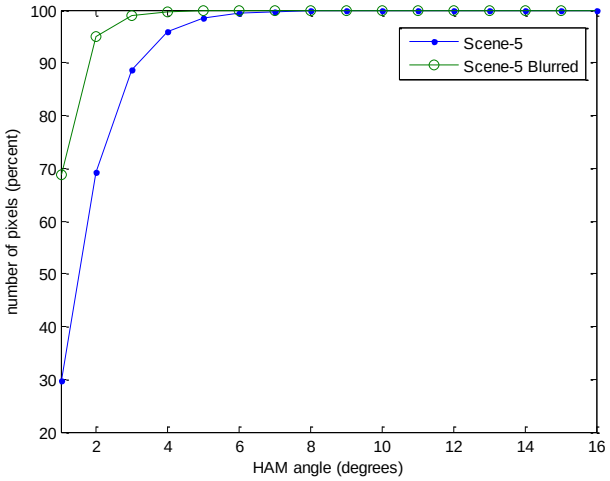


Figure 37. Values on the ordinate show the proportion of spectrally-blurred and original Scene-5 pixels whose HAM angles are smaller than the respective numbers on the abscissa.

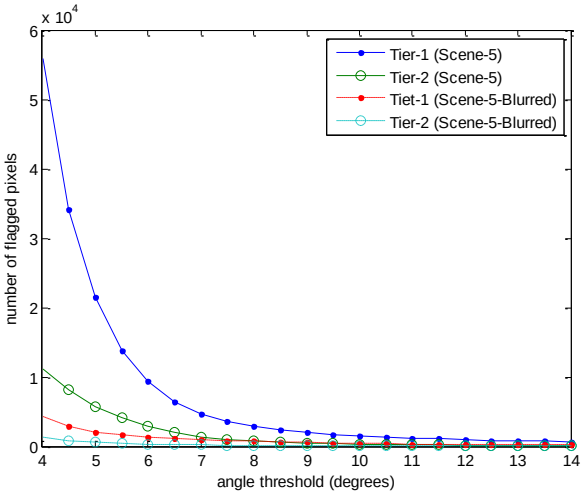


Figure 38. Comparison of number of designated pixels that exceed the angle threshold for original and spectrally-blurred Scene-5. $\kappa$ equals 2° for Tier-2.

Figures 39 through 45 show the effect of spectral blurring on the spectrum of seven pixels in the Scene-5 image. The spectra of designated pixels before and after the spectral transformation are plotted next to each other. In each plot, the two spectra are normalized with respect to their maximum intensities; however, it should be noted that the total energy contained in each spectrum for a given pixel is the same. The impact on the spectra caused by the spectral blurring/smearing is significant in changing the shape of the pixel spectrum. The "spectral intensity" labeling the ordinate of Figures 39 through 46 are normalized values. For all figures thereafter, the spectral intensity labels represent relative values and can be compared between these figures. It should be recognized that these figures are for spectrally-blurred images which changes the original pixel spectra for the images. In subsection 4.4, anomalous source detection for spectrally-blurred images are investigated by simulation. Due to the three-tier algorithms not requiring knowledge of the scene or anomalies, the anomaly detection performance seemingly is not noticeably degraded by the spectral blurring.

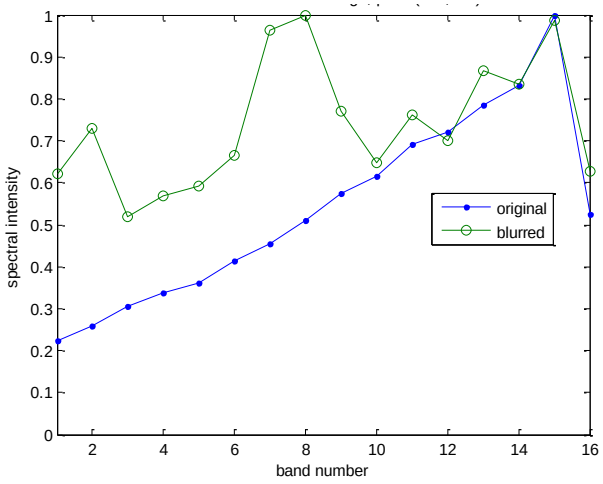


Figure 39. Normalized spectra at pixel location (520,200) of the 16-band Scene-5 image and its spectrally-blurred version. Each spectrum is normalized with respect to its peak value.

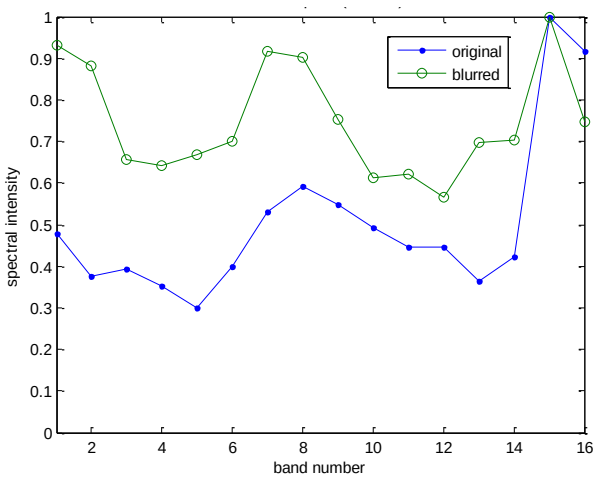


Figure 40. Normalized spectra at pixel location (80,840) of the 16-band Scene-5 image and its spectrally-blurred version. Each spectrum is normalized with respect to its peak value.

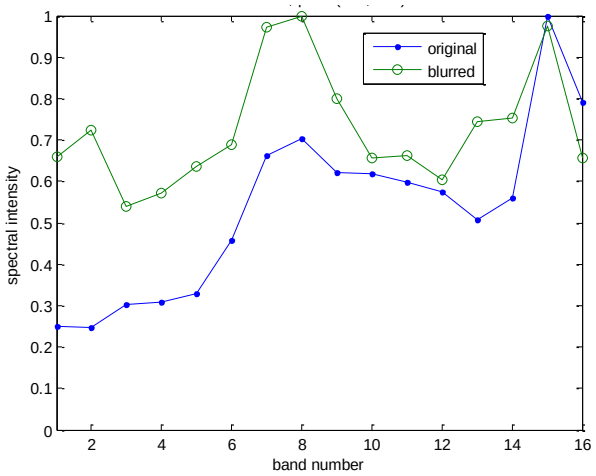


Figure 41. Normalized spectra at pixel location (880,550) of the 16-band Scene-5 image and its spectrally-blurred version. Each spectrum is normalized with respect to its peak value.

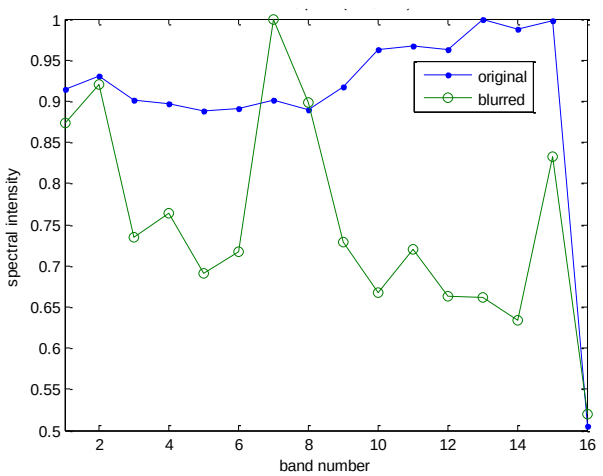


Figure 42. Normalized spectra at pixel location (920,850) of the 16-band Scene-5 image and its spectrally-blurred version. Each spectrum is normalized with respect to its peak value.

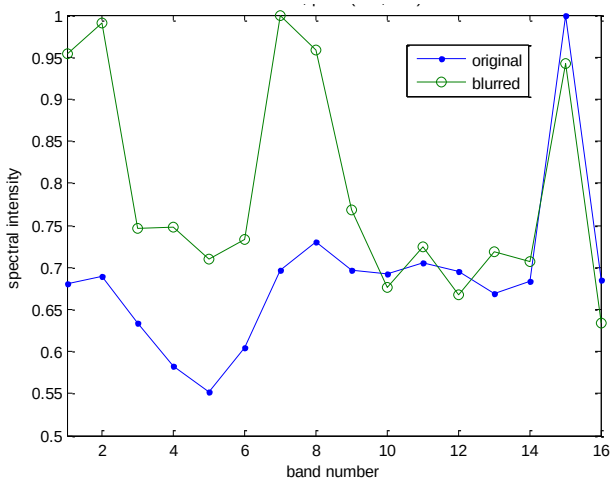


Figure 43. Normalized spectra at pixel location (940,870) of the 16-band Scene-5 image and its spectrally-blurred version. Each spectrum is normalized with respect to its peak value.

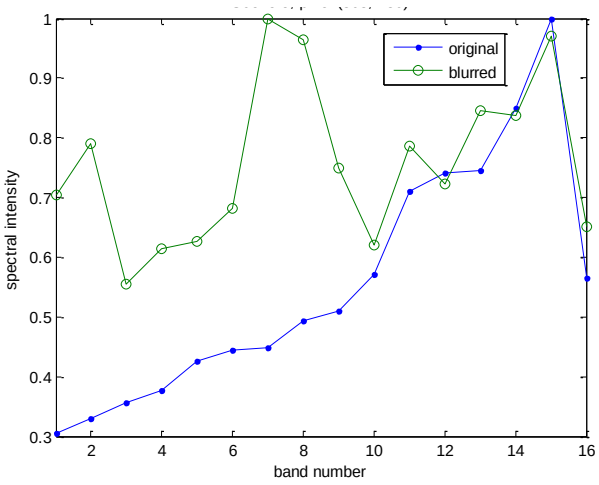


Figure 44. Normalized spectra at pixel location (863,130) of the 16-band Scene-5 image and its spectrally-blurred version. Each spectrum is normalized with respect to its peak value.

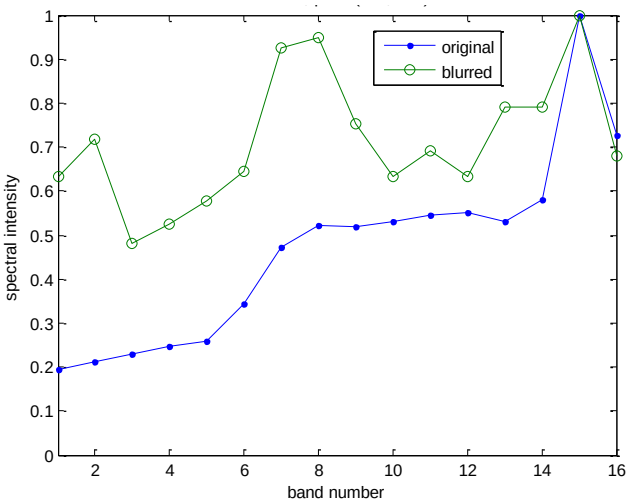


Figure 45. Normalized spectra at pixel location (760,550) of the 16-band Scene-5 image and its spectrally-blurred version. Each spectrum is normalized with respect to its peak value.

### 4.4. Anomalous Source Detection Simulations

Rather than using spectra from highly dissimilar objects such as a truck, tank, camouflage paint, etc. for anomalous sources, it was decided to select four pixels from the 16-band Scene-7 image that were dissimilar from each other. These spectra, denoted as Type-1, Type-2, Type-3, and Type-4, are presented in Figure 46 with their pixel locations identified. In order to evaluate the detection performance of the three-tier anomalous source detection process, one thousand anomalous sources were implanted in the 16-band Scene-5 image as follows:

- Anomalous sources were equally divided between Type-1, Type-2, Type-3, and Type-4.
- Anomalous pixel locations were randomly selected.
- Minimum allowable separation between implanted anomalous pixels was set such that no two pixels are located in the same kernel.[13]
- Spectrum of each selected pixel was replaced with a mixture of its original spectrum and the spectrum of the anomalous source to create an anomalous-source contaminated pixel.
- The mixture factor, *a*, was varied from 20% to 100% in 10% increments.
- Total energy in an anomalous-source contaminated pixel is equal to the total energy in the original pixel in accordance with Eq. (2).

[13] Two kernels can overlap, but two anomalous pixels cannot be adjacent to one another.

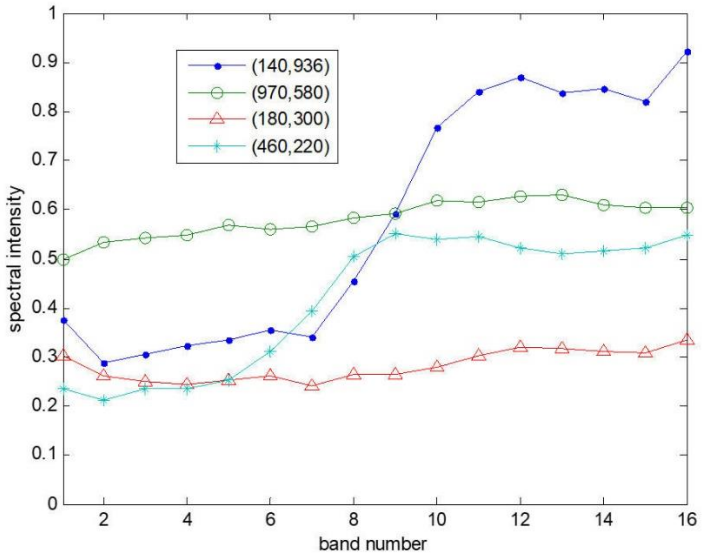


Figure 46. The spectra of four pixels from 16-band Scene-7 image which were utilized as anomalous sources. Type-1 through Type-4 anomalous sources are plotted with, respectively, dots, circles, triangles, and stars.

Table 2. Anomalous source classification matrix.

| Anomalous Source | Anomaly Declared | Classification | Meaning |
|---|---|---|---|
| Present | Yes | True-Positive | Anomaly Found |
| Present | No | False-Negative | Anomaly Missed |
| Not Present | Yes | False-Positive | False Alarm |
| Not Present | No | True-Negative | No Anomaly |

The 16-band Scene-5 image was processed, with $a$ = 100%, using the spectral transformation procedure to produce the spectrally-blurred 16-band Scene5 image. The aforementioned anomalies were implanted in the image. The resultant spectrally-blurred Scene-5 image was subsequently processed with the three-tier anomaly detection process; 951 anomalous pixel locations were correctly identified (true positives), 49 anomalies went undetected (false negatives), and no false-positives were declared (zero false alarms). Table 2 provides the anomalous source classification matrix used in this analysis. Figures 47 through 60 show spectra plots for nine-pixel kernels centered at fifteen representative correctly-identified (true-positive) anomalous pixels in the spectrally-blurred 16-band Scene-5 image.

In each of these figures, the spectrum of the anomalous core pixel is denoted with dots and the spectra of the eight pixels of the surrounding ring are also shown. The HAM angle between the spectrum of the core pixel (anomaly) and the mean-spectrum of the kernel ring, and the largest angle between the spectra of the eight pixels of the kernel ring and its mean-spectrum are stated in each figure caption. Visual inspect of Figure 47 gives the appearance that the core pixel is anomalous while the core pixel spectrum in Figure 48 looks like it is not anomalous. Nevertheless,

the Tier-3 process recognizes that the HAM angle between the spectrum of the core pixel and the mean-spectrum of the kernel ring is adequately greater than largest angle between the spectra of the eight pixels of the kernel ring and its mean-spectrum and consequently declares this pixel anomalous (true positive). Examination of Figures 47–60 illustrate the remarkable ability of the three-tier algorithms to correctly identify anomalies even when a human analyst most likely could not make the identification. Figures 61 through 65 show the spectra plots of nine-pixel kernels centered at five pixels which comprise a subset of the 49 undetected anomalies (false negatives). It was observed that virtually all Type-1 and Type-2 anomalies (499 out of 500) were detected and virtually all the false-negatives involved Type-3 and Type-4 anomalies.

Since the subpixel-scale anomaly may not fully replace the original pixel, the observed spectral signal will be a mixture of the original and anomaly signals (see Eq. (2)) and can be considered to have formed a contaminated pixel. In Figure 66, the contamination factor was changed from 20% ($a$ = 0.2) to 100% ($a$ = 1) in 10% increments. For each setting of the mixture factor, a new 16-band Scene-5 image was generated and was then transformed to the corresponding spectrally-blurred 16-band Scene-5 image. The locations and anomaly type of the one-thousand implanted anomalies were kept unchanged as the contamination factor $a$ was varied. The anomaly detection process was applied to each of the generated spectrally-blurred sixteen-band Scene-5 images. The probability of detection and false alarms were computed for each of these images. The effect of contamination factor on probability of detection is shown in Figure 66. Example probabilities of detection for contamination factors of $a = 1,\ 0.8,$ and $0.6$ are, respectively, 0.96, 0.86, and 0.67, and the probability of a false alarm was determined to be zero for all nine contaminated images. Figures 67 through 72 show the spectra of six true-positive detected anomalous pixels for contamination factors of $a = 1,\ 0.8,$ and $0.6$ in the spectrally-blurred sixteen-band Scene-5 image. The ability of the three-tier anomaly detection process is arguably extraordinary upon examination of these figures, especially Figure 69.

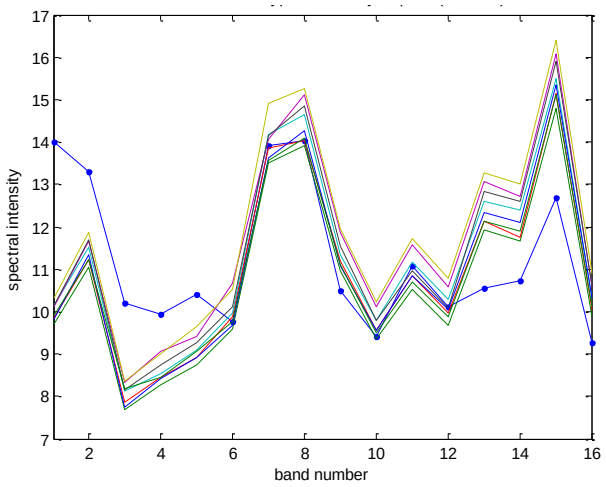


Figure 47. Kernel spectra for a true-positive Type-3 anomalous source implanted at pixel location (582,597). The HAM angle between the spectrum of the core pixel and the mean-spectrum of the ring is 8.4°, while the largest angle between the spectra of the eight pixels of the ring and its mean-spectrum is 0.8°.

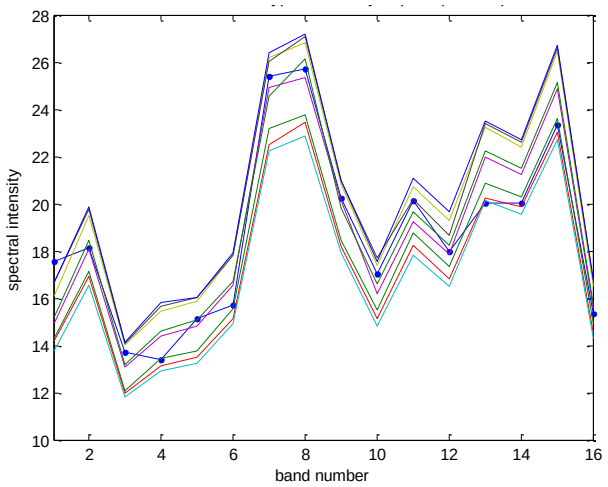


Figure 48. Kernel spectra for a true-positive Type-3 anomalous source implanted at pixel location (494,371). The HAM angle between the spectrum of the core pixel and the mean-spectrum of the ring is 3.2°, while the largest angle between the spectra of the eight pixels of the ring and its mean-spectrum is 0.8°.

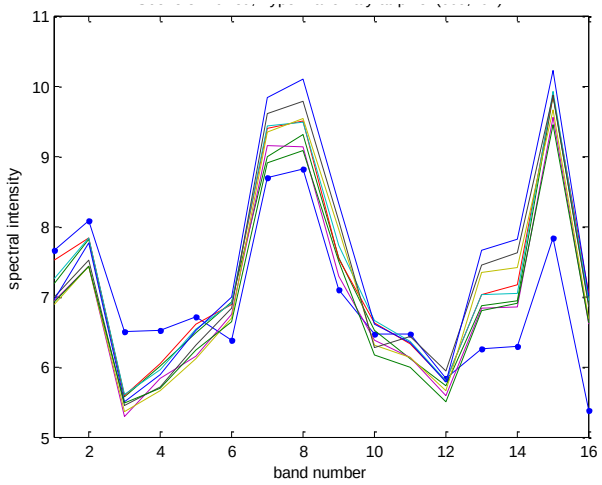


Figure 49. Kernel spectra for a true-positive Type-3 anomalous source implanted at pixel location (609,404). The HAM angle between the spectrum of the core pixel and the mean-spectrum of the ring is 6.2°, while the largest angle between the spectra of the eight pixels of the ring and its mean-spectrum is 1.5°.

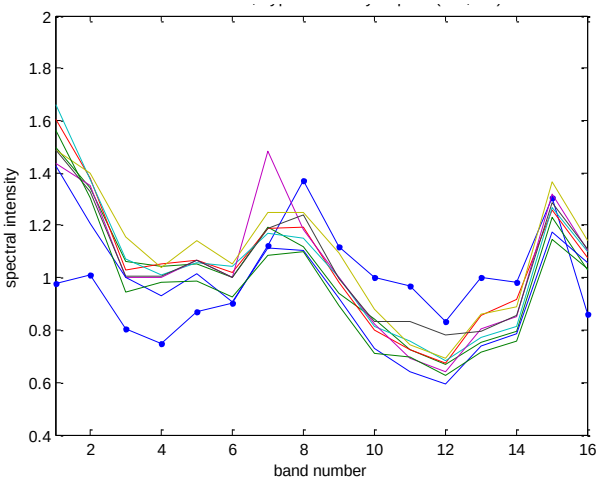


Figure 50. Kernel spectra for a true-positive Type-3 anomalous source implanted at pixel location (645,738). The HAM angle between the spectrum of the core pixel and the mean-spectrum of the ring is 12.7°, while the largest angle between the spectra of the eight pixels of the ring and its mean-spectrum is 3.9°.

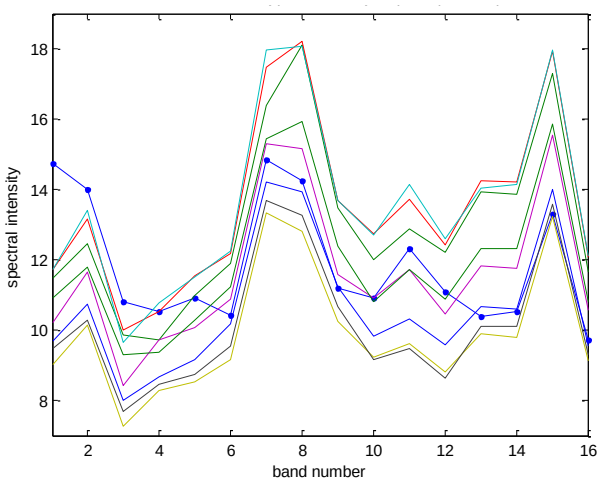


Figure 51. Kernel spectra for a true-positive Type-3 anomalous source implanted at pixel location (661,386). The HAM angle between the spectrum of the core pixel and the mean-spectrum of the ring is 8°, while the largest angle between the spectra of the eight pixels of the ring and its mean-spectrum is 1.8°.

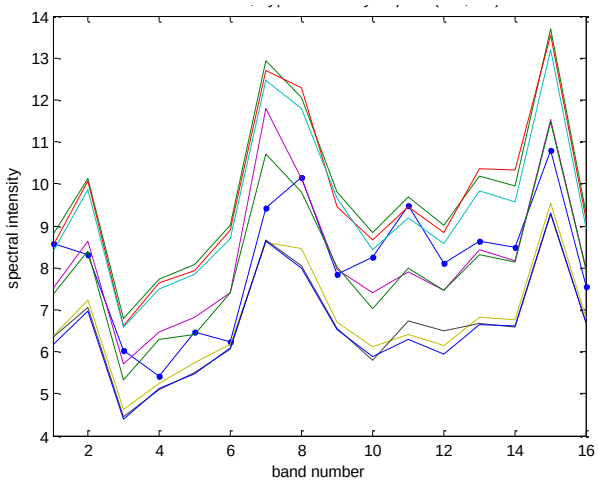


Figure 52. Kernel spectra for a true-positive Type-1 anomalous source implanted at pixel location (596,344). The HAM angle between the spectrum of the core pixel and the mean-spectrum of the ring is 5.6°, while the largest angle between the spectra of the eight pixels of the ring and its mean-spectrum is 1.6°.

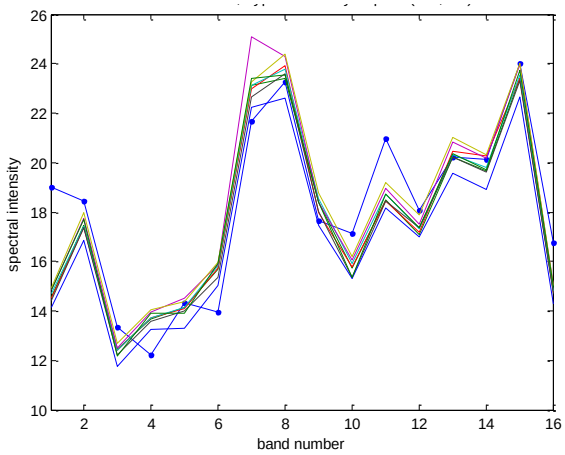


Figure 53. Kernel spectra for a true-positive Type-1 anomalous source implanted at pixel location (504,479). The HAM angle between the spectrum of the core pixel and the mean-spectrum of the ring is 4.9°, while the largest angle between the spectra of the eight pixels of the ring and its mean-spectrum is 1.1°.

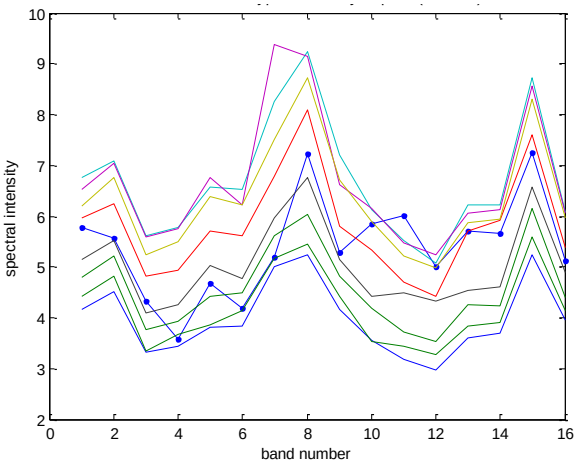


Figure 54. Kernel spectra for a true-positive Type-1 anomalous source implanted at pixel location (689,356). The HAM angle between the spectrum of the core pixel and the mean-spectrum of the ring is 8.3°, while the largest angle between the spectra of the eight pixels of the ring and its mean-spectrum is 2.7°.

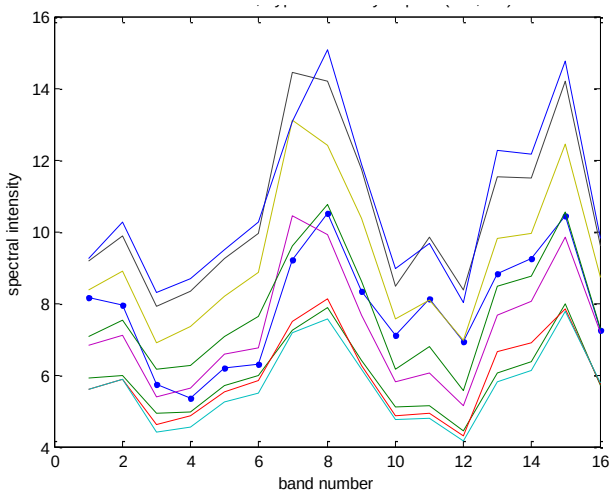


Figure 55. Kernel spectra for a true-positive Type-1 anomalous source implanted at pixel location (526,622). The HAM angle between the spectrum of the core pixel and the mean-spectrum of the ring is 5.5°, while the largest angle between the spectra of the eight pixels of the ring and its mean-spectrum is 2.6°.

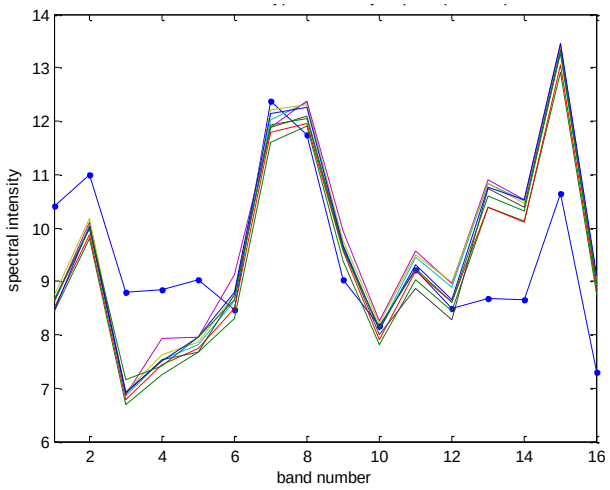


Figure 56. Kernel spectra for a true-positive Type-2 anomalous source implanted at pixel location (568,346). The HAM angle between the spectrum of the core pixel and the mean-spectrum of the ring is 7.9°, while the largest angle between the spectra of the eight pixels of the ring and its mean-spectrum is 0.9°.

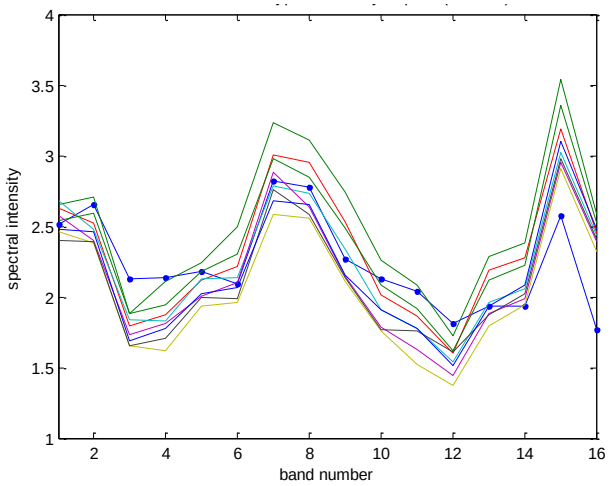


Figure 57. Kernel spectra for a true-positive Type-2 anomalous source implanted at pixel location (595,793). The HAM angle between the spectrum of the core pixel and the mean-spectrum of the ring is 7°, while the largest angle between the spectra of the eight pixels of the ring and its mean-spectrum is 2.1°.

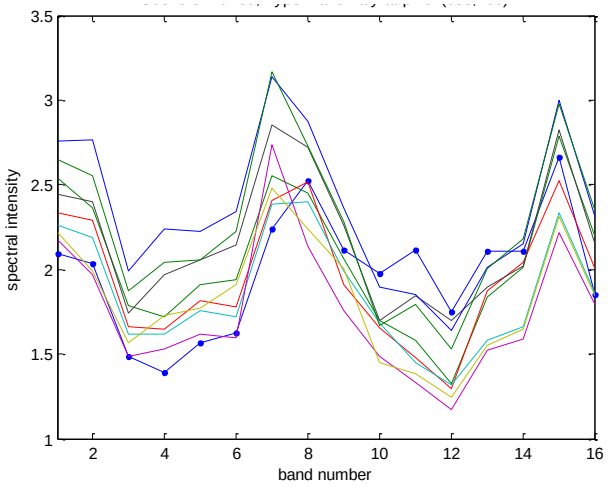


Figure 58. Kernel spectra for a true-positive Type-1 anomalous source implanted at pixel location (635,760). The HAM angle between the spectrum of the core pixel and the mean-spectrum of the ring is 8.6°, while the largest angle between the spectra of the eight pixels of the ring and its mean-spectrum is 3.4°.

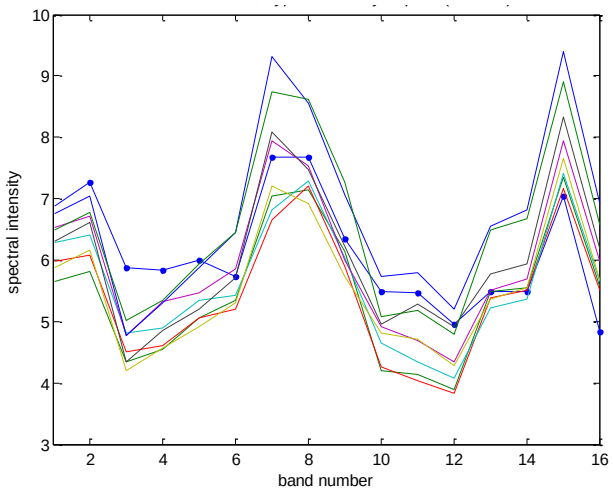


Figure 59. Kernel spectra for a true-positive Type-2 anomalous source implanted at pixel location (336,696). The HAM angle between the spectrum of the core pixel and the mean-spectrum of the ring is 6.3°, while the largest angle between the spectra of the eight pixels of the ring and its mean-spectrum is 2.5°.

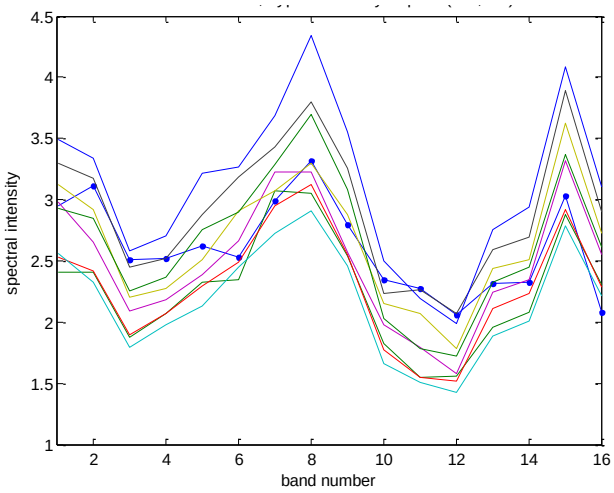


Figure 60. Kernel spectra for a true-positive Type-2 anomalous source implanted at pixel location (572,665). The HAM angle between the spectrum of the core pixel and the mean-spectrum of the ring is 6.1°, while the largest angle between the spectra of the eight pixels of the ring and its mean-spectrum is 2.5°.

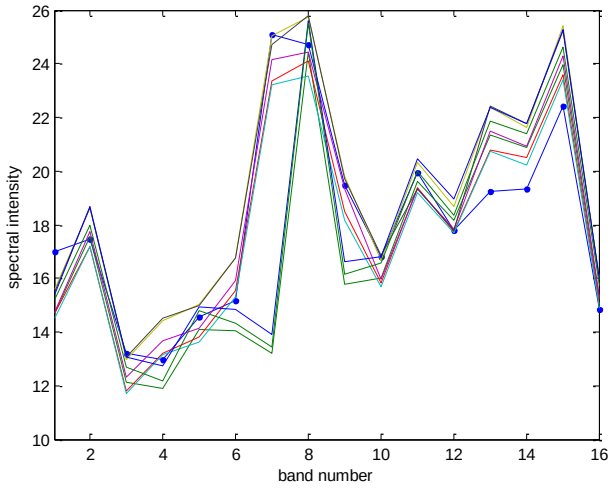


Figure 61. Kernel spectra for a false-negative Type-4 anomalous source implanted at pixel location (513,301). The HAM angle between the spectrum of the core pixel and the mean-spectrum of the ring is 8.8°, while the largest angle between the spectra of the eight pixels of the ring and its mean-spectrum is 5.5°.

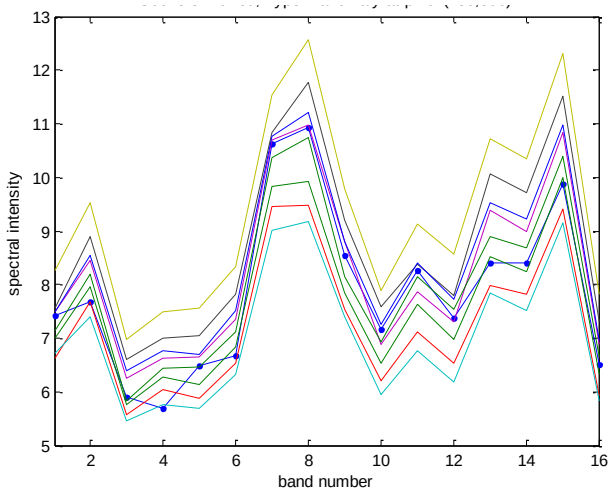


Figure 62. Kernel spectra for a false-negative Type-4 anomalous source implanted at pixel location (430,306). The HAM angle between the spectrum of the core pixel and the mean-spectrum of the ring is 1.8°, while the largest angle between the spectra of the eight pixels of the ring and its mean-spectrum is 1.1°.

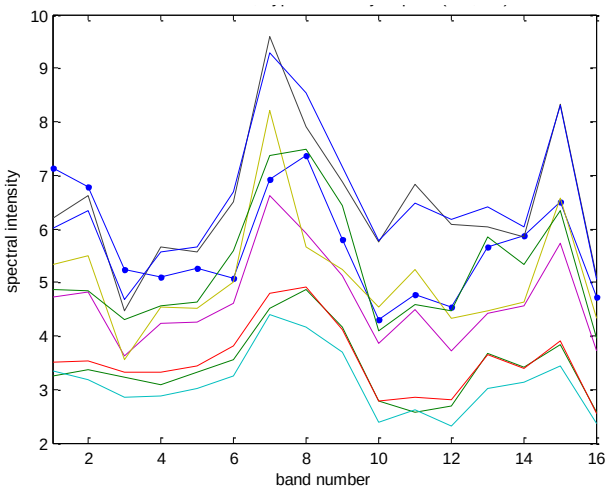


Figure 63. Kernel spectra for a false-negative Type-3 anomalous source implanted at pixel location (627,308). The HAM angle between the spectrum of the core pixel and the mean-spectrum of the ring is 9.7°, while the largest angle between the spectra of the eight pixels of the ring and its mean-spectrum is 5°.

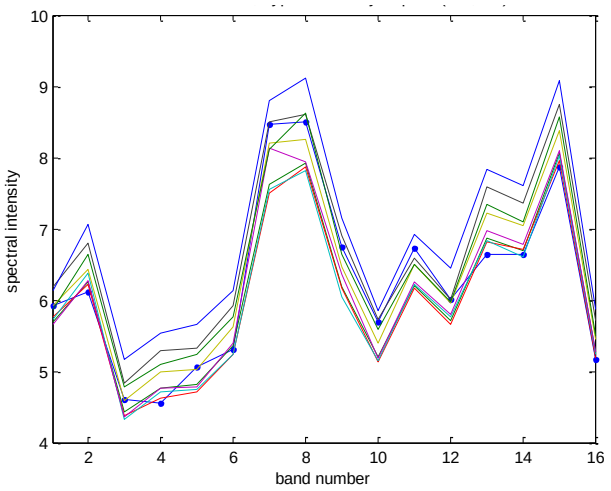


Figure 64. Kernel spectra for a false-negative Type-4 anomalous source implanted at pixel location (477,373). The HAM angle between the spectrum of the core pixel and the mean-spectrum of the ring is 1.5°, while the largest angle between the spectra of the eight pixels of the ring and its mean-spectrum is 0.9°.

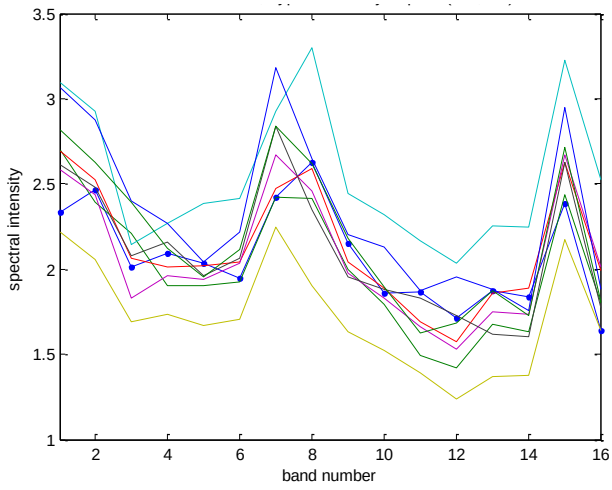


Figure 65. Kernel spectra for a false-negative Type-2 anomalous source implanted at pixel location (645,374). The HAM angle between the spectrum of the core pixel and the mean-spectrum of the ring is 6.2°, while the largest angle between the spectra of the eight pixels of the ring and its mean-spectrum is 3.8°.

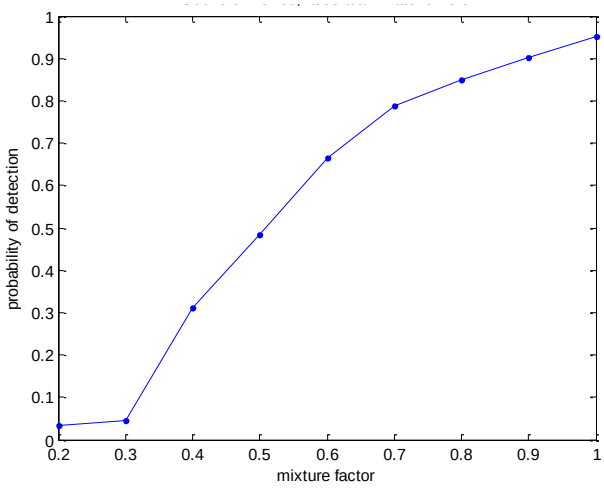


Figure 66. Effect of anomaly contamination factor *a* on probability of detection for the spectrally-blurred Scene-5 image. Zero false positives or false alarms were detected. All four anomaly types, evenly divided, comprised the one thousand imbedded anomalies.

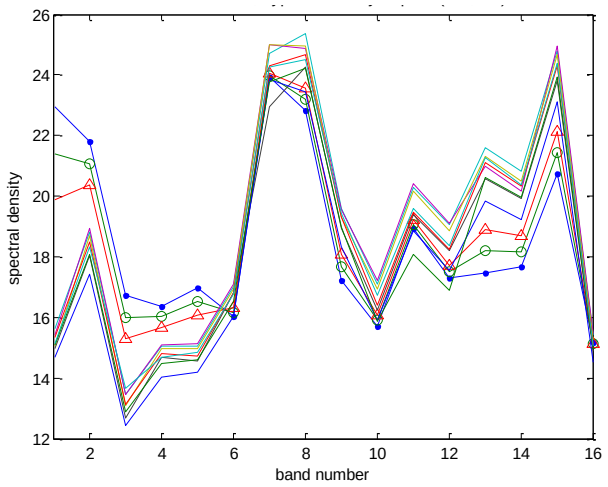


Figure 67. Kernel spectra for a true-positive Type-3 anomalous source implanted at pixel location (306,303) with contamination factors of $a=1$ (dots), $a=0.8$ (circles), and $a=0.6$ (triangles). The HAM angles between the spectrum of the core pixel and the mean-spectrum of the ring are 5.5°, 4.3°, and 3.3°, respectively, for these contamination factors while the largest angle between the spectra of the eight pixels of the ring and its mean-spectrum is 2.2°.

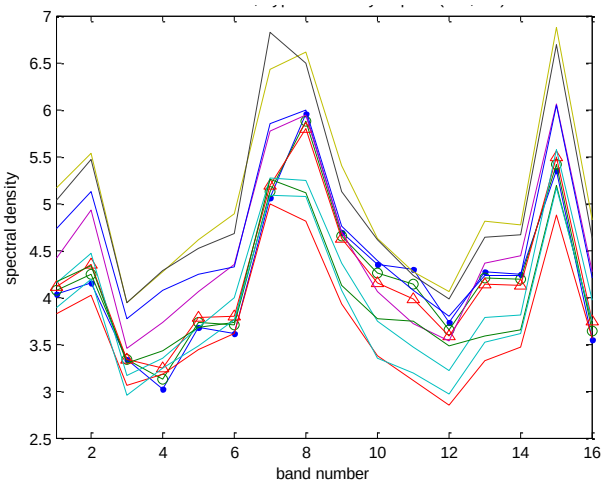


Figure 68. Kernel spectra for a true-positive Type-3 anomalous source implanted at pixel location (387,314) with contamination factors of $a=1$ (dots), $a=0.8$ (circles), and $a=0.6$ (triangles). The HAM angles between the spectrum of the core pixel and the mean-spectrum of the ring are 5.4°, 4.3°, and 3.3°, respectively, for these contamination factors while the largest angle between the spectra of the eight pixels of the ring and its mean-spectrum is 1.9°.

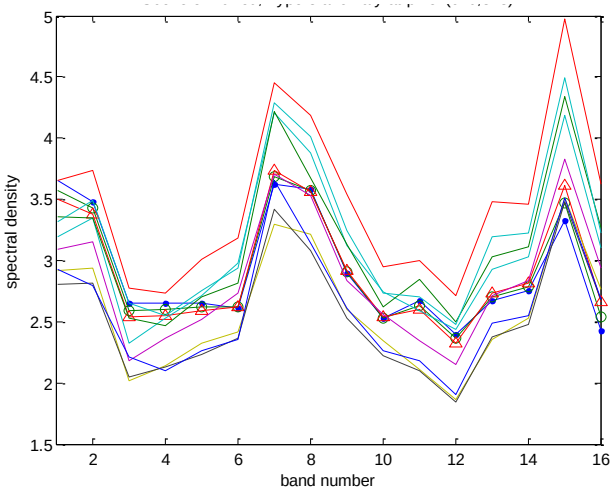


Figure 69. Kernel spectra for a true-positive Type-3 anomalous source implanted at pixel location (640,328) with contamination factors of $a=1$ (dots), $a=0.8$ (circles), and $a=0.6$ (triangles). The HAM angles between the spectrum of the core pixel and the mean-spectrum of the ring are 6.1°, 4.9°, and 3.8°, respectively, for these contamination factors while the largest angle between the spectra of the eight pixels of the ring and its mean-spectrum is 1.9°.

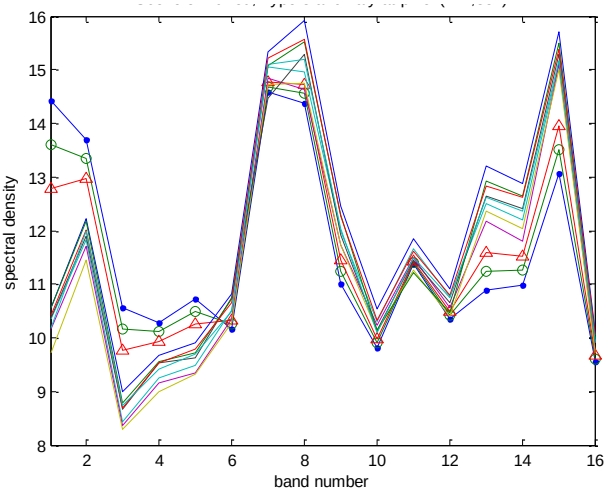


Figure 70. Kernel spectra for a true-positive Type-3 anomalous source implanted at pixel location (444,354) with contamination factors of $a=1$ (dots), $a=0.8$ (circles), and $a=0.6$ (triangles). The HAM angles between the spectrum of the core pixel and the mean-spectrum of the ring are 7.6°, 6.1°, and 4.6°, respectively, for these contamination factors while the largest angle between the spectra of the eight pixels of the ring and its mean-spectrum is 0.8°.

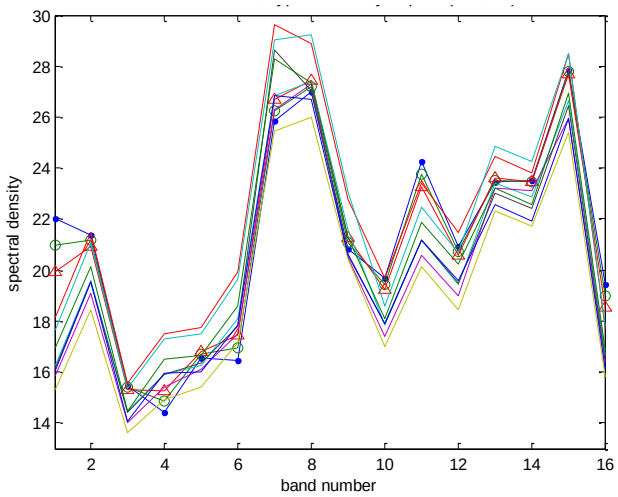


Figure 71. Kernel spectra for a true-positive Type-1 anomalous source implanted at pixel location (520,533) with contamination factors of $a = 1$ (dots), $a = 0.8$ (circles), and $a = 0.6$ (triangles). The HAM angles between the spectrum of the core pixel and the mean-spectrum of the ring are 5.1°, 4.1°, and 3.0°, respectively, for these contamination factors while the largest angle between the spectra of the eight pixels of the ring and its mean-spectrum is 1.0°.

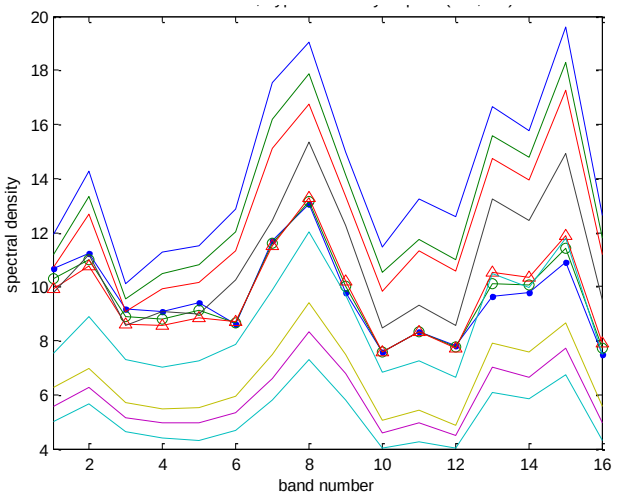


Figure 72. Kernel spectra for a true-positive Type-2 anomalous source implanted at pixel location (338,546) with contamination factors of $a = 1$ (dots), $a = 0.8$ (circles), and $a = 0.6$ (triangles). The HAM angles between the spectrum of the core pixel and the mean-spectrum of the ring are 7.2°, 5.7°, and 4.3°, respectively, for these contamination factors while the largest angle between the spectra of the eight pixels of the ring and its mean-spectrum is 2.9°.

## 5. Potential Practical Applications using the Three-Tier Method

Among the myriad of potential practical applications of the Three-Tier Method include such areas as agriculture, military, ocean surveillance, medical, and manufacturing. In agriculture, an example is searching for diseased areas in crop fields in its early stages which could have large impact on crop yield. Aircraft flying over hostile territory could locate possible threats long before conventional system can detect the threats. Drones carrying cameras could potentially locate IEDs, camouflaged materials and vehicles, and hiding personnel. Aircraft and ships could use the Three-Tier Method to look for boats, downed aircraft, debris, small craft, near-surface submerged boats, etc. Manufacturing applications may include looking for tiny flaws in sheet materials, chromatic error in items, etc. Scanning for anomalous areas on the human body could result in the detection of disease onset much earlier than currently possible.

## 6. Conclusions and Future Research

The spectral corruption or blurring resulting from the design of the telecentric phenoptic hyperspectral camera has been shown to be nontrivial and likely not useful for precision hyperspectral measurements. The principal question considered in this investigation was what impact does this camera's characteristic have on the detection of subpixel-scale anomalous objects. Intuitively, it would seem that such spectral corruption of a hyperspectral image would degrade the detection of anomalous objects. However, this investigation strongly indicates that the new Johnson-Heidary HAM algorithmic method for anomaly detection described in the prior section is quite insensitive to spectral corruption of the image. The former Heidary-Johnson incongruence

method for detection of subpixel-scale anomalous objects would inherently be more sensitivity to spectral corruption of images than the new Johnson-Heidary HAM method. The reasons are that the incongruence method (i) requires the user to adjust, ad hoc, the threshold and selection of spectral bands, (ii) utilizes a constant threshold value, and (iii) is quite computationally intensive while the HAM method (iv) is a three tier process that greatly decreases the computational load, (v) has the user set a rather insensitive scaling factor, and (vi) autonomously determines the decision threshold for every pixel examined in the final tier. Furthermore, the detection and false alarms performance for the incongruence method is arguably grossly inferior to the HAM method.

The Johnson-Heidary HAM method for locating subpixel-scale anomalous objects was contrived to be generally oblivious to the nature of anomalous objects and to the structure of the image, i.e., the method's algorithms require no a priori knowledge of the anomalous objects or the image scene. The process examines individual 3x3 pixel kernels in the scene to determine if the core pixel is anomalous or not. Computationally, all of the kernels comprising the image can be processed in parallel if the software/hardware implementation is capable. Potentially, real-time scene analysis can be realized.

Future research is planned to investigate (i) autonomous determination of the scaling constants $\kappa$ and $\chi$, (ii) detection when anomalous objects are partially in adjacent pixels, (iii) unresolved anomalous objects that extend over several pixels, (iv) coarse estimation of the nature of the anomalous objects such as if they are metal, natural material, plastics, etc. and (v) software/hardware implementation. In addition, a wide range of multispectral and hyperspectral images will be analyzed to further validate the process.

## Acknowledgments

Alabama A&M University and Army Research Office (ARO) (W911NF-15-1-0531) each provided, in part, the funding for this investigation.